Jet Physics at the Tevatron

Anwar A. Bhatti[1] and Don Lincoln[2]

[1]Laboratory of Experimental High-Energy Physics, The Rockefeller University, New York, New York 10065; email: bhatti@fnal.gov

[2]Fermi National Accelerator Laboratory, Batavia, Illinois 60510; email: lincoln@fnal.gov

Annu. Rev. Nucl. Part. Sci. 2010. 60:267–97

First published online as a Review in Advance on July 16, 2010

The *Annual Review of Nuclear and Particle Science* is online at nucl.annualreviews.org

This article's doi: 10.1146/annurev.nucl.012809.104430

0163-8998/10/1123-0267$20.00

Key Words

QCD, jet cross section, dijet resonance search, compositeness, extra dimensions

Abstract

Jets have been used to verify the theory of quantum chromodynamics (QCD), measure the structure of the proton, and search for physics beyond the Standard Model. In this article, we review the current status of jet physics at the Tevatron, a $\sqrt{s} = 1.96$ TeV $p\bar{p}$ collider at the Fermi National Accelerator Laboratory. We report on recent measurements of the inclusive jet production cross section, dijet production measurements, and the results of searches for physics beyond the Standard Model using jets.

Contents

1. INTRODUCTION

The theory of quantum chromodynamics (QCD) (1) is currently the best description of the fundamental strong force. This theory describes the color interaction between quarks as being mediated by gluons, the vector bosons of the strong force. QCD has been successfully tested in e^+e^- (2), ep (3), pp (4), and $p\bar{p}$ (5) collisions.

One of the basic properties of QCD is that its coupling strength α_s decreases with the energy of the interaction, and at sufficiently high energies, QCD calculations can be performed using perturbation theory in powers of α_s (6). Currently, these perturbative QCD (pQCD) calculations are available at next-to-leading order (NLO) for many processes and, in some cases, at next-to-next-to-leading order (NNLO). Leading-order (LO) calculations, supplemented with parton shower calculations (7), are used in several Monte Carlo event generators (8, 9). Also, matrix element generators that match NLO calculations of rates for QCD processes with a parton shower Monte Carlo event generator are also available (10), but only a limited number of processes have been implemented.

The pQCD calculations result in a small number of partons in the final state, whereas experimenters observe jets of particles. These jets retain the kinematic properties (energy and momentum) of the parent partons (quarks or gluons). To facilitate comparison between data and calculation, researchers have devised jet-finding algorithms that are insensitive to the difficult-to-calculate low-energy phenomena that govern the transition from low-multiplicity partons to high-multiplicity particle final states. There are several jet-finding algorithms, and the details of the measurements are sensitive to the choice of algorithm.

Although events in which jets are created are used for a detailed understanding of the strong force, it is also possible that such events could reveal new physical phenomena, including quark substructure (compositeness), extra spatial dimensions, and new particles that decay into jets.

Because of their high energy, jets can probe very small distances. At the Tevatron, the highest-p_T jets can probe distances down to $\mathcal{O}(10^{-17})$ cm.

In 2001, the Fermilab Tevatron $p\bar{p}$ collider commenced Run II, with a collision energy of 1.96 TeV. By contrast, the 1992–1996 Run I had an energy of 1.8 TeV. Even this relatively small increase in energy leads to a substantial increase in jet production with large transverse momentum, p_T, by approximately a factor of three at $p_T = 500$ GeV/c. The beam intensity of Run II is much higher than that of Run I due to the addition of the Main Injector and the Recycler Ring to the Fermilab accelerator complex (11). Also, both the CDF (12) and DØ detectors (13) were upgraded. The results reported here utilize an order-of-magnitude-higher integrated luminosity than reported previously (5).

2. PERTURBATIVE QUANTUM CHROMODYNAMICS

The theory of QCD describes the behavior of those particles (quarks q and gluons g) that experience the strong force. It is broadly modeled on the theory of quantum electrodynamics (QED), which describes the interactions between electrically charged particles. However, unlike the electrically neutral photon of QED, the gluons (the force-mediating bosons of the strong interaction) carry the strong charge. This fact greatly increases the complexity in calculating the behavior of matter undergoing interactions via the strong force.

The mathematical techniques required to make these calculations can be found in textbooks (e.g., 14). Instead of giving an exhaustive description of those techniques here, we focus on those aspects of the calculations employed most frequently in the experimental analysis, thereby clarifying the phenomena that experimentalists investigate.

At high energies, the strong interactions between two hadrons can be factorized into three components: (*a*) the probability of finding the partons in the hadrons, (*b*) the interaction between quasi-free partons, and (*c*) fragmentation and hadronization of the final-state partons. The process is schematically shown in **Figure 1**. The cross section of the hadron-hadron scattering with four-momenta P_1 and P_2 can be written as (14)

$$\sigma(P_1, P_2) = \sum_{i,j} \int dx_1 \int dx_2 \, f_i(x_1, \mu_F^2) f_j(x_2, \mu_F^2) \hat{\sigma}_{ij}[p_1, p_2, \alpha_s(\mu_R^2), Q^2/\mu_F^2, Q^2/\mu_R^2]. \qquad 1.$$

The hard interaction between partons i and j is given by $\hat{\sigma}_{ij}$, where $p_1 = x_1 P_1$ and $p_2 = x_2 P_2$ are four-momenta of the two partons. This interaction is independent of the incoming hadrons' structure and can be calculated with pQCD. The function $f_i(x, \mu_F^2)$ is the probability of finding a parton i with momentum fraction x at the scale μ_F, and it is known as the parton distribution function (PDF). The sum i, j is over the partons in the two respective hadrons; α_s is the strong coupling constant; μ_R is the renormalization scale, which is used to remove nonphysical infinities inherent in fixed-order calculations; and Q is the characteristic scale of the interaction and is related to some physical scale in the interaction, such as the p_T of the leading jet.

This factorization of hadron-hadron interactions into a short-distance interaction (hard interaction) and a long-distance interaction (PDF) is done at an arbitrary energy scale μ_F. A parton emitted below the scale μ_F is considered to be part of the hadron structure and thus is described by the PDFs. The hadron structure is measured by many different experiments, especially lepton-hadron scattering experiments. The PDFs are determined by fitting these data and are parameterized at a scale μ_0. The QCD evolution equations (7), currently available at NNLO in perturbation theory, are used to evolve these PDFs to any different scale μ. The cross section is a convolution of the PDFs and the parton-level cross section, and to be consistent, both must be calculated to the same order in perturbation theory. A complete calculation, including all orders

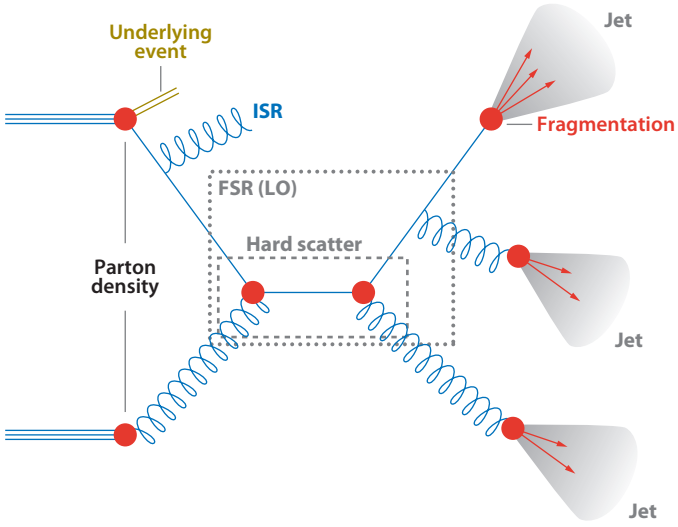

Figure 1

Stylized hadron-hadron collision, with relevant features labeled. Note that a leading-order (LO) calculation of the hard scatter (*dashed gray line*) will assign a jet to final-state radiation (FSR) that would be included in the hard scatter calculation by a next-to-leading-order calculation (*dotted gray line*). Abbreviation: ISR, initial-state radiation.

in the perturbation series, must be independent of μ_F, but a fixed-order calculation depends on this choice. To evaluate the sensitivity to μ_F, this scale is usually varied up and down by a factor of two. Scale dependencies are expected to decline with the addition of higher-order terms in the calculation.

In **Figure 2**, examples of LO and NLO Feynman diagrams for jet production are shown. At NLO, the jet cross section receives contributions from virtual corrections to the two-parton final state and from real corrections from the three-parton final state. Both contributions are divergent, but the sum is finite. An NLO pQCD calculation can describe up to three jets in the final state. For inclusive jet production, many different implementations of NLO pQCD calculations are available (15–18). All these programs use Monte Carlo integration techniques to calculate the real and virtual contribution to the cross sections. The EKS program (15) calculates the cross sections for user-predefined cuts on transverse momentum and rapidity ranges. JETRAD (16) and NLOJet++ (17) generate parton events with weights (both positive and negative), and thus full event kinematics are available to the user for jet clustering, detector acceptance calculations, and study of any other distribution. These programs require a huge amount of processing power to reach the desired precision. A large fraction of this processing power is consumed in evaluating the PDFs. In the FastNLO program (18), the convolution in Equation 1 is modified to a product of a perturbatively calculable piece $\sigma_{n,i,k,l,m}(\mu)$ that is calculated using NLOJet++, the strong coupling constant, and a function $F_a(x_1, x_1, \mu_F)$ that depends on only the PDFs and the factorization scale μ_F. The time-consuming piece σ is calculated only once. The function F_a is calculated on a grid of different values of x_1, x_2, and μ_F only once, and it is interpolated between those points while evaluating the full cross section. This procedure significantly speeds up the calculations.

Near threshold, the phase space for the emission of real gluons is limited, and large logarithmic corrections to the above cross-section calculation may arise from the incomplete cancellation of infrared (IR) divergences against the virtual gluon emission contributions. For jet production, these corrections are expected to contribute at very high x, where parton distributions fall very

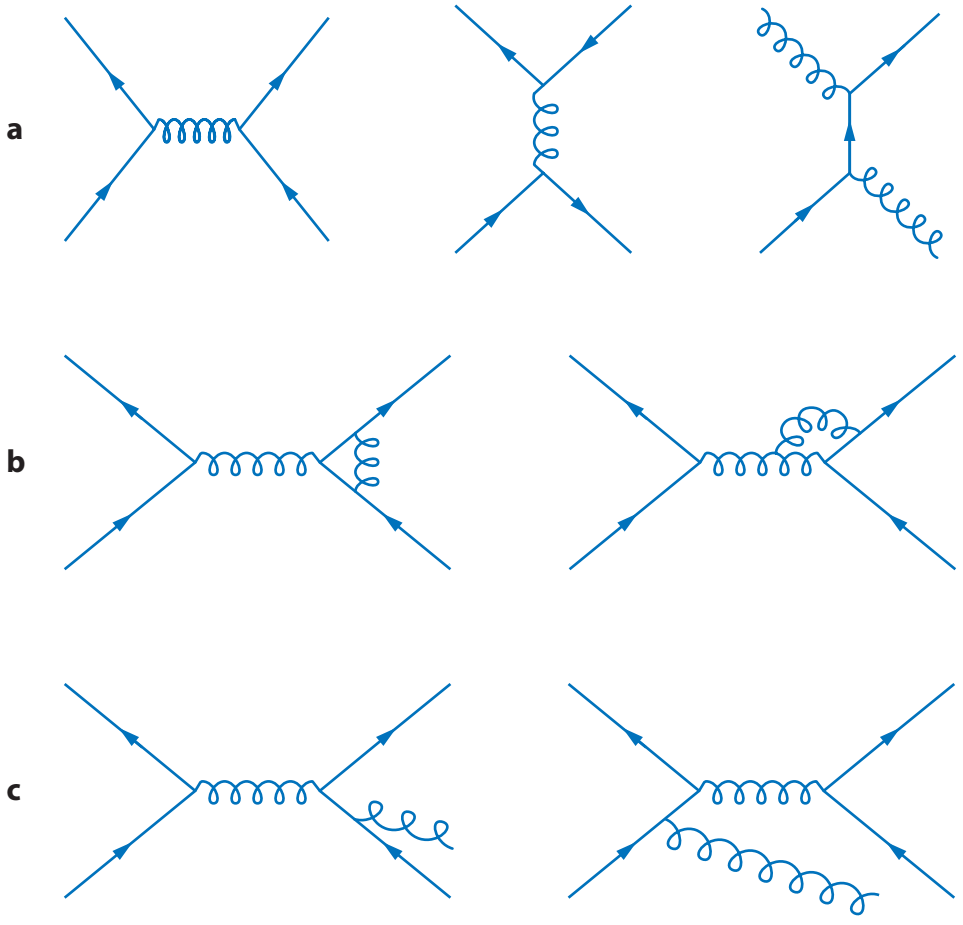

Figure 2

(*a*) Leading-order tree diagrams. (*b*) Next-to-leading-order loop diagrams. (*c*) Next-to-leading-order tree diagrams.

steeply. For the inclusive jet cross section, these threshold corrections have been calculated to NNLO at next-to-leading-logarithmic accuracy (19) and are found to be small. However, the corrected cross section shows a substantial reduction of the scale μ_F and μ_R dependence.

The partons radiate when they pass through a color field. In this type of radiation, two forms dominate: collinear and soft radiation. Collinear radiation is in the direction of the parent parton, whereas soft radiation is simply low-energy emission. Such soft and collinear radiation can be calculated in a leading-logarithmic approximation to all orders, and this algorithm is a crucial component of event generators. In this formalism, a gluon radiates another gluon or converts into a $q\bar{q}$ pair according to DGLAP (Dokshitzer-Gribov-Lipatov-Altarelli-Parisi) splitting functions (7) that depend on α_s and on a variable z, which describes the energy sharing between two daughter partons. Similarly, a quark or an antiquark can radiate a gluon that radiates further. This sequential radiation results in a shower of partons. The radiation process is continued until the parton virtual mass t is smaller than a mass scale t_0. This simple procedure is augmented by angular ordering; that is, each subsequent emission is required to have a smaller angle so as to simulate color

coherence effects. Color coherence leads to suppression of soft gluon radiation in certain regions of phase space. In the final-state showers, the radiation is limited to a cone defined by color flow lines, and the emission angle at each branch point is smaller than the previous emission angle. Partons with a virtual mass $t \leq t_0 \sim 1$ GeV/c^2 are combined into hadrons by means of a phenomenological hadronization model. The hadronization models have been tuned to reproduce the jet structure observed at e^+e^- colliders. The showering process described above is used for radiation from outgoing partons, which is known as final-state radiation (FSR). For radiation from incoming partons, known as initial-state radiation (ISR), the event generators use so-called backward evolution. First, the momentum fractions x_1 and x_2 of partons participating in the hard interaction are determined. Second, the parton shower that preceded the hard interaction is subsequently reconstructed, evolving partons from the hard interaction scale Q backward in time toward smaller Q, at which the PDF f is evaluated. The color coherence in ISR is slightly more complicated but still follows the same angular ordering. Interference between ISR and FSR is implemented in HERWIG but not in PYTHIA. The independent variable t, through which the evolution of $\alpha_s(t)$ is parameterized, is not unique. In the PYTHIA showering algorithm, the squared mass m^2 of the branching parton is used as the evolution variable. HERWIG uses $t = m^2/[2z(1-z)]$, where $z = E_b/E_a$ is the ratio of daughter parton energy (E_b) to parent parton energy (E_a). In recent versions of PYTHIA, $t = p_{\mathrm{T}}$ of the branching parton is also available as the evolution variable.

Occasionally, the radiated parton is at a sufficiently large angle to the parent parton and carries enough energy that it leads to an identifiable jet. Because such jets are typically of lower p_{T}, they do not dominate the event kinematics. However, this lower-p_{T} radiation becomes important in studies of jet multiplicity. This part of ISR/FSR can either be considered as a component of the hard scatter $\hat{\sigma}_{ij}$ or can be treated independently. For instance, **Figure 1** shows one box surrounding the LO scatter and another box surrounding an NLO diagram. At NLO pQCD, one parton emitted from either an incoming or outgoing parton is part of the short-distance hard cross section $\hat{\sigma}_{ij}$. In LO event generators, these parton emissions are treated quasi-independently of the hard scatter and are part of the leading-log showering process.

The partons from the incoming hadrons that do not participate in the hardest scatter in an event also interact, but these interactions are normally soft. The particles produced in these multiparton interactions are, on average, isotropically distributed in the allowed $y - \phi$[1] space and can overlap with the jets produced in the hard interactions. Being soft, multiparton interactions are in the nonperturbative regime and thus are implemented in event generators using QCD-inspired phenomenological models. The parameters of these multiparton interaction models have been tuned to reproduce the transverse energy and multiplicity distributions of the particles observed far away from the hard jets in collider data (20, 21). The beam remnants, namely the partons that do not participate in either hard or multiparton interactions, go along the beam direction. However, they do carry color, and to become color singlets, they must exchange (soft) partons with the rest of the event. The particles produced in multiparton interactions and from the hadronization of beam remnants collectively constitute the underlying event.

As described above, pQCD predictions for jet production are available at NLO at the parton level only. These predictions cannot, in principle, be compared directly with the data, which are

[1]The important kinematic variables are the rapidity $y = \frac{1}{2} \ln \frac{E+p_z}{E-p_z}$; the azimuthal angle $\phi = \tan^{-1} \frac{p_y}{p_x}$; and the transverse momentum $p_T = \sqrt{p_x^2 + p_y^2}$, where a particle or jet has a four-momentum (E, p_x, p_y, and p_z) and the positive z is defined by the proton beam's direction, positive y is up, and the x direction is that required to make a right-handed coordinate system. In addition, the pseudorapidity $\eta = -\ln[\tan(\theta/2)]$ is sometimes used, where θ is the polar angle, measured with respect to the proton beam axis. The boost rapidity is defined as $y_{boost} = 0.5|y_1 + y_2|$.

available at the particle level because these parton-level calculations do not include hadronization effects and the contribution from the underlying event. However, event generators include hadronization, underlying-event energy, and ISR/FSR to all orders in the leading-log approximation, but the hard interaction is calculated at LO only. Thus, to compare data with QCD predictions, a hybrid scheme is generally used. The parton-level NLO calculations are correcting for the underlying-event and hadronization effects before they are compared with data. One can determine these corrections with Monte Carlo event generators by comparing the jets obtained by clustering the pQCD partons with the jets obtained by clustering the particles after the hadronization process. The parton jets are obtained from Monte Carlo events in which the underlying-event simulation (multiple parton scattering) has been turned off.

Over the past decade, there has been a great deal of progress in simulating high jet-multiplicity events using tree-level matrix elements. In ALPGEN (22), events with the exclusive parton multiplicities $n = 2, 3, 4$, and 5 are generated by using matrix elements from pQCD at the tree level. To include the effect of soft and collinear emission to all orders (albeit in the leading-log approximation), these events are passed through a showering program, such as PYTHIA. The phase spaces of the matrix elements and the parton showering program overlap. In particular, showering programs occasionally generate hard partons, which can lead to a state that has already been generated by the matrix element. To avoid this double counting, a matching criterion is used. For example, in ALPGEN for inclusive N jet production, the number of jets produced by clustering the partons that are produced by the matrix element must be the same as the number of those produced after the showering for $n \leq N$. The events that do not satisfy this condition are rejected. For the $n = N$ parton state, the showering algorithm is allowed to produce a higher jet-multiplicity state. The spectra from each different multiplicity are combined to form the full spectrum. SHERPA (23) employs a different matching procedure (24) in which parton showers above a cutoff k_T-like measure (Equation 4) are vetoed. Both ALPGEN and SHERPA have been extensively tested at the Tevatron in W/Z + jet production, but we do not discuss these studies here due to space constraints (25).

Although lepton-nucleon deep-inelastic scattering (DIS) experiments can precisely measure the quark content of the proton, this precision is not achievable for the gluon, especially at high x. At low x, the gluon distribution can be determined precisely using QCD scaling violation in DIS data. Studying the high-x gluon distribution functions requires data from hadron-hadron scattering. The effect of including Tevatron jet data in global fits to determine PDFs is described in Section 5.3.

3. JET CLUSTERING ALGORITHMS

Because partons carry the strong charge, they are not directly observable. A parton showers into many partons, which combine to form a large number of particles that travel in roughly the same directions as the initial parton. The kinematic properties of the initial parton can be inferred from the jet of collimated particles. For this inference, these particles or partons must be clustered into a jet by an algorithm. In pQCD, at NLO and higher orders, a jet algorithm is needed to define physics observables that are well defined, that is, that are soft/collinear safe. Jet algorithms are run on a few partons generated in pQCD calculations to construct such variables. Experimentally, the final-state particles are observed as tracks in the tracker systems or as towers of energy in the calorimeter. These tracks or towers must also be combined into a reconstructed jet so that they can be compared to the parton produced in the hard interaction. In the following sections, we collectively refer to (*a*) partons in a pQCD calculation, (*b*) partons or (*c*) particles produced in Monte Carlo event generators, (*d*) towers or (*e*) tracks, or (*f*) reconstructed particles observed in a detector as the objects that function as input for a clustering algorithm.

For a valid comparison between observations and theoretical predictions, the clustering algorithm must satisfy some basic criteria (26, 28). The algorithm must be safe against soft (IR) and collinear radiation, invariant to boosts along the beam direction, and insensitive to the nonperturbative hadronization effects. In an algorithm that is not safe against soft/collinear radiation, the virtual and real contributions in pQCD calculations do not cancel completely, and thus the predicted cross sections are ill defined. One should be able to run the same algorithm on the detector calorimeter towers or tracks, particles or the multiparton state from event generators, and partons in fixed-order pQCD calculations and obtain sensible results. Experimentally, a jet clustering algorithm should be insensitive to the energy from additional hadron-hadron collisions in the same bunch crossing that overlaps the energy from hard interactions, and it should not consume too many computer resources such as processing power. Finally, the algorithm must be completely specified.

Commonly used jet-finding algorithms can be divided into two categories: (*a*) cone clustering algorithms and (*b*) pair-wise recombination algorithms. With a few exceptions, only cone clustering algorithms have been used at hadron colliders. The cone clustering algorithms used prior to the Tevatron Run II were not IR/collinear safe (26, 27), and it was proposed to add an additional seed at the midpoint of stable cones. This made the new algorithm IR/collinear safe to NLO for the inclusive jet cross-section measurement. For other physics observables, it is either safe at LO only or unsafe at all orders (28). Various issues related to jet reconstruction are extensively discussed in a recent review (29).

3.1. Cone Clustering Algorithm

For jet studies in Run II, both the CDF and DØ Collaborations are using the Midpoint Algorithm, as laid out by the QCD Workshop recommendations (26), but the two implementations differ in some details. Below we describe the implementation of this algorithm by the CDF Collaboration.

The clustering process starts with a list of all objects to be clustered. In simulated events, all the particles or partons are included without a p_{T} threshold. However, in data, the calorimeter towers are required to have $p_{\mathrm{T}} \geq 100$ MeV/c to minimize the effect of detector noise. From the initial list, a second list of seed objects is made with the requirement that the p_{T} of the objects exceed a fixed threshold of 1.0 GeV/c. At each seed location, the four-momentum of the cluster is determined by summing the four-momenta of all the objects within a distance $R = \sqrt{(y - y_c)^2 + (\phi - \phi_c)^2}$ from the seed (y_c, ϕ_c). The four-momenta are summed using the E-scheme (26)

$$(E, p_x, p_y, p_z) = \sum_i (E, p_x, p_y, p_z)_i, \qquad 2.$$

$$p_{\mathrm{T}} = \sqrt{p_x^2 + p_y^2}, y_c = \frac{1}{2} \ln \left(\frac{E + p_z}{E - p_z} \right), \phi_c = \tan^{-1}(p_y / p_x). \qquad 3.$$

This yields massive jets with $m^2 = E^2 - p^2$ and is different from the Snowmass scheme (30) used in Run I, where the clustering centroid was defined as the E_{T}-weighted average of η and ϕ and jets were massless. Using the center of the cluster as a new seed location, the process is iterated until the center of the circle (y_c, ϕ_c) coincides with the position of the cluster four-momentum.

After all the stable cones have been identified, beginning with real seeds, an additional search for stable cones takes place in which the midpoints between the initial set of stable cones are used as seed locations. This cone-finding algorithm allows that the same object may be part of many cones. The shared objects are uniquely assigned to a single cone via a split-merge algorithm, as specified in Reference 26. If two stable cones share objects, the shared energy is compared to the energy of the lower-p_{T} cone. If the ratio of the shared transverse energy to the transverse energy of

the lower-p_T cone is higher than an energy fraction f_{merge}, the two cones are merged. Otherwise, on the basis of proximity, the shared objects are assigned to the nearest cone. The two collaborations use different values of f_{merge}: CDF uses $f_{merge} = 0.75$, and DØ uses $f_{merge} = 0.50$. This split-merge procedure may lead to jets that are not circular in $y - \phi$ space. After all the objects above threshold have been uniquely assigned to a stable cone, the jet kinematics are determined through the same E-scheme.

A cone clustering algorithm can be made IR safe to all orders if a stable cone is evaluated at each point in $y - \phi$ space. Such an algorithm is very processing-power intensive even when the number of particles is modest, and thus its use is not practical beyond some parton-level pQCD calculations. Recently, a new seedless cone clustering algorithm that is IR and collinear safe to all orders in perturbation theory was proposed. The Seedless Infrared Safe Cone algorithm (31) uses the fact that a circle enclosing a set of particles can be moved around such that two of the particles lie on its circumference. Consequently, all stable circles can be reconstructed by considering all possible pairs of particles. After determining all the stable circles the algorithm merges and splits the stable circles to uniquely assign the particles to a single circle. This algorithm is fast and has been used at the Tevatron for comparison purposes only.

3.2. Pair-Wise Clustering Algorithm

The cone algorithm combines all the objects within a distance R from the seed. In contrast, the recombination algorithms combine pairs of objects based on some measure d_{ij} and are an attempt to undo the showering of partons. The k_T algorithm (32, 33) begins with a list of protojets given by four-momentum (E, p_x, p_y, and p_z). All the objects to be clustered are considered to be protojets. The transverse momentum p_T, rapidity y, and azimuthal angle ϕ of a protojet are calculated using Equation 3.

For each protojet i and the pair i, j, where $i \neq j$, d_i and d_{ij} are defined as

$$d_i = p_{T,i}^2;$$
$$d_{ij} = \min(p_{T,i}^{2p}, p_{T,j}^{2p}) \frac{(y_i - y_j)^2 + (\phi_i - \phi_j)^2}{D^2}, \quad 4.$$

where D is the parameter that controls the size of the jet. For the k_T algorithm, the parameter $p = 1$. The algorithm determines the minimum $d_{\min}$ of the d_i and all the d_{ij}. If $d_{\min} = d_i$, the protojet is not mergeable and is promoted to a jet. Otherwise, the protojets i and j are merged into a single protojet with the four-momentum $(E_{ij}, \vec{p}_{ij}) = (E_i + E_j, \vec{p}_i + \vec{p}_j)$. The process is repeated until no protojets are left.

The k_T algorithm has been extensively used at e^+e^- and ep colliders. At hadron colliders, the environment is more challenging. The energy from multiparton interactions, beam remnants, and pileup can contribute to the jets and must be taken into account. The large particle multiplicity observed in hadron-hadron collisions requires substantial computer power to process an event. Thus, the use of the k_T algorithm has been limited at hadron colliders. The DØ Collaboration measured the inclusive jet cross section in Run I (34) using this algorithm. In the Tevatron Run II, the k_T algorithm was used only by the CDF Collaboration to measure the inclusive jet cross section (described in Section 5.2).

Recently, two additional recombination algorithms that use $p = 0$ (Cambridge-Aachen) (35) and $p = -1$ (anti-k_T) (36) in Equation 4 were proposed. The Cambridge-Aachen algorithm combines particles based only on their relative distance. The anti-k_T algorithm combines the highest-p_T objects in the events first. This process leads to circular jets, which like the cone jets have well-defined areas. Thus far, these algorithms have not been used at the Tevatron.

4. JET ENERGY SCALE DETERMINATION

At the Tevatron, jets are generally measured with a calorimeter, which is sensitive to both charged and neutral particles. Both CDF and DØ utilize sampling calorimeters, which measure only a small fraction of the energy of the particles. This observed energy is multiplied by a calibration constant so that it is equal to the sum of the energies of the incident particles. The calorimeter response is different for hadrons, photons, electrons, and muons. For hadrons, the response depends on the momentum and the type of the particles, whereas for photons and electrons it is almost momentum independent. Muons normally deposit a small amount of energy (~few GeV) in the calorimeter, which is almost independent of the muon momentum. Neutrinos escape without interacting and lead to an imbalance in the measured p_T in the event. The observed jet energy must be corrected for the calorimeter response and other detector effects. CDF and DØ employ different techniques to determine these jet energy scale corrections. The CDF Collaboration's technique (37) depends on an accurate modeling of the calorimeter response to single particles and on knowledge of the p_T spectrum of the particles in a jet, whereas the DØ technique is data driven and utilizes the fact that in photon-jet events $p_{T,jet} = p_{T,\gamma}$ (38). These techniques are used to calibrate the central region of the calorimeter, where the tracking system is available to measure the charged-particle momentum and where the calorimeter response is uniform.

The calorimeter response was extended to other regions ($|\eta| < 0.1$, $|\eta| > 0.7$ for CDF and $|\eta| > 0.5$ for DØ) by using dijet balancing to scale the jet energy response in the other regions to the one in the central region. The energy from additional $p\bar{p}$ interactions in the same bunch crossing was subtracted; the correction is based on the number of reconstructed primary vertices in an event. For cone jets, this correction is determined from minimum bias events by summing the energy in towers in a cone of radius R placed randomly in the calorimeter. The procedure for k_T jets is described in Section 5.2.

4.1. Photon-Jet Balancing

In this technique, the jet energy is determined by scaling the measured jet p_T to the photon's p_T in photon-jet events. The photon energy is measured by the electromagnetic (EM) calorimeter, which is linear and has very good energy resolution. In the approximation of $2 \to 2$ scattering, the jet transverse energy p_T is equal to the photon p_T. The real situation is a little more complicated due to the presence of ISR, the energy not clustered in the jet, and contributions to the clustered jet from the multiple parton interactions. To be insensitive to these effects (especially ISR), DØ evaluates the missing p_T ($\not\!\!E_T$) projection fraction along the photon direction using

$$R_{bad} = 1 + \frac{\vec{\not\!\!E}_T \cdot \vec{p}_{T,\gamma}}{p^2_{T,\gamma}}. \quad 5.$$

The hadronic recoil correction factor, R_{bad}, is the scale factor to the entire recoil system. By requiring that the jet be back to back with the photon, and in the absence of any additional jet(s) in the event, R_{bad} is almost equal to the jet response. The derived response is expressed in the jet energy E' determined from the p_T of the photon and the position of the balancing jet using $E' \equiv p^\gamma_T / \sin\theta^{jet}$, as both p^γ_T and the direction of the jet are accurately measured. Thus, E' provides a better estimate of the jet energy than does the direct jet energy measurement by the calorimeter. It is preferred over jet p_T because the calorimeter response depends on the energy of the incident particles; therefore, the parameterization of calorimeter response in E' is more natural.

The EM calorimeter is calibrated using the electrons from Z boson decays such that the reconstructed Z boson mass is equal to the world average (39). The EM calorimeter response to

electrons and photons is similar, but not the same, because photons begin their shower later than electrons. This difference is small and is evaluated using simulated events at $p_T = 100$ GeV/c. The estimated uncertainty on the photon energy scale is 0.5% at low E' and 0.8% at high E'. Using this procedure, the DØ Collaboration has achieved a 1% accuracy on the jet energy scale in photon-jet events. The current statistics of the $\gamma+$ jets sample limit the direct measurement of the jet energy corrections in the central region to $E' < 350$ GeV. The response is extrapolated to higher energies using Monte Carlo, which has been tuned to the data. The correction to a single jet with a given algorithm and size is deduced from R_{had} using simulated events.

The calorimeter response to jets depends on their flavor, as the particle spectrum and multiplicity for quark-initiated and gluon-initiated jets are different. The jet energy scale corrections determined from $\gamma+$ jet events are valid only for the flavor composition of $\gamma+$ jet events. Event topologies with different flavor composition have different jet energy scale corrections. Indeed, DØ tuned the single-pion response in their detector simulator to data and used PYTHIA to generate photon-quark, photon-gluon, and dijet events. The author of this study (38) found that the gluon jet response was 8% (2%) lower for jets with 20 GeV (500 GeV) of energy. In QCD jet production, the fraction of gluon-initiated jets changes with jet p_T, so the corrections were adjusted to account for this variation in flavor composition. With these additional corrections, the uncertainty on the jet energy scale was reduced to an unprecedentedly small value.

4.2. Jet Corrections Using Single-Particle Response

Another approach to determine the jet energy correction is based on a knowledge of the calorimeter response to each particle that makes up a jet. The CDF Collaboration measured the calorimeter response to charged hadrons and electrons using both $p\bar{p}$ collider and test-beam data. The calorimeter simulation was tuned to reproduce the measured response. The calorimeter response to a jet was determined by a convolution of the single-particle response with the type and momentum distribution of particles constituting a jet, as given by a fragmentation model. CDF used QCD dijet events with the PYTHIA fragmentation model to measure the default jet corrections. The PYTHIA fragmentation model agreed well with the particle p_T and multiplicity distributions in a jet measured in $p\bar{p}$ data. The HERWIG event generator was used to cross-check the PYTHIA fragmentation functions, and the results that were determined using two generators agreed well. In this procedure, the difference in calorimeter response to gluon-initiated and quark-initiated jets is automatically included. Although this procedure requires a detailed knowledge of the calorimeter response and a well-tuned simulation, it has the advantages that (*a*) the correction can be easily determined for any event topology over the entire kinematic range and (*b*) real and simulated data have the same corrections and thus can be treated on an equal footing.

5. INCLUSIVE JET CROSS SECTION

The inclusive jet cross-section measurement (40–45) has been used to test QCD and to search for physics beyond the Standard Model by searching for an excess of events at high p_T. During Run I at $\sqrt{s} = 1.8$ TeV, the search was limited by both theoretical and experimental systematic uncertainties, even with an integrated luminosity of 100 pb^{-1}. The uncertainty on the jet energy scale dominated the experimental uncertainty. NLO pQCD calculations (15–17) significantly reduced the dependence on the factorization and renormalization scales, and the remaining dependence was ~10%—almost independent of jet p_T for $p_T > 100$ GeV/c. The jet cross section is not very sensitive to nonperturbative hadronization effects. The underlying event contributes approximately 2 GeV/c of p_T to a jet and thus is significant only at low p_T. The main theoretical uncertainty

arises from uncertainty in the PDFs, especially for high-x gluons. Unfortunately, inclusive jet production is the only process in which the high-x gluon distribution can be directly measured. The other possible process, photon-jet production, has a limited reach in x, and the associated theoretical uncertainties are large. The gluon distributions are also measured from lepton-proton scattering data through QCD scaling violations, but these measurements are also limited to low-x values. Because of these limitations, the Run II inclusive jet cross section has been used primarily to constrain the gluon content of the proton. The data at high y are particularly useful as they probe high x at lower Q values, where the contribution of physics beyond the Standard Model, if any, is negligible.

Due to the higher center-of-mass energy and much larger integrated luminosity, Run II jet measurements extend the jet spectrum to higher jet p_T, compared to the Run I measurements, by approximately 200 GeV/c. Both CDF and DØ implemented an improved jet clustering algorithm. The jet clustering algorithms used in Run II are IR/collinear safe at least to the order of the available pQCD calculations. An accurate determination of the calorimeter response from the $p\bar{p}$ data as well as a refinement in the techniques to determine the jet energy scale have led to reduced systematic uncertainty compared to Run I. In previous inclusive measurements, the hadronization effects were ignored, as they were much smaller than both the experimental and theoretical uncertainties. In Run II, both collaborations have evaluated the effect of hadronization and corrected the parton-level pQCD calculation. Also, the pQCD calculations are corrected for the energy from the underlying event, which is determined using tuned event generators. In contrast, in Run I, energy from the underlying event was removed from jets in data.

The CDF Collaboration measured the inclusive jet cross section using (*a*) the cone clustering (46) algorithm, where the cone size $R = 0.7$, and (*b*) the k_T clustering algorithm, where $D = 0.5$, 0.7, and 1.0 (47). The DØ Collaboration recently published the inclusive jet cross section (48) using the cone clustering algorithm, where the cone size $R = 0.7$. These three measurements are described below.

5.1. Measurement Using Cone Clustering Algorithm

The most common jet-finding algorithms at the Tevatron are variations of the cone clustering algorithm.

5.1.1. DØ Collaboration. The DØ Collaboration analyzed 0.7 fb^{-1} of data taken from 2004 to 2005 to measure the inclusive jet cross section for $p_T > 50$ GeV/c in six rapidity bins, $|\Delta y| = 0.4$ wide, over the range $0 < |y| < 2.4$. The data were collected by triggering on a jet passing a p_T threshold. Six triggers with p_T thresholds of 15, 25, 45, 65, 95, and 125 GeV/c were used to collect data. Due to high production rates, only predetermined fractions of the lower-threshold triggers were recorded. The efficiency for triggering on jet events was measured by using data collected with a muon trigger that did not rely on calorimeter activity. These different jet triggers were combined to form the full p_T spectrum, with each trigger contributing to a unique p_T range. Only those data for which the trigger efficiency was >98% were used. The events were required to have a reconstructed primary vertex, and the position of the $p\bar{p}$ interaction had to be within 50 cm of the detector center along the beam direction. These requirements ensured that the jets followed the projective geometry of the calorimeter, and thus their energy was accurately measured. The consequence of these requirements was a reduction of only $7.0 \pm 0.5\%$ in the integrated luminosity. The primary vertex was reconstructed using charged-particle tracks that were measured using silicon microstrip and scintillating fiber detectors located inside a 2-T solenoidal magnetic field (13).

The triggered data include events containing cosmic-ray interactions, beam halo, and detector noise. These contributions are mostly asymmetric and lead to a large imbalance in the momentum in the plane transverse to the beam direction, $\not\!\!E_T$. In contrast, for QCD jet production, $\not\!\!E_T$ is ideally zero, apart from a small neutrino contribution. In QCD events, $\not\!\!E_T$ arises mainly from fluctuations in calorimeter response and is much smaller than the total energy observed in the detector. Most of these background events are removed by requiring the ratio of $\not\!\!E_T$ to the transverse momentum of the leading jet to be small. Remaining backgrounds are removed by requiring that the shape of energy deposition in the calorimeters be consistent with the expected shape from a hadronic jet. The shape of energy deposition for a jet is very different from that of the energy deposited by a cosmic muon or a beam halo particle, as a jet consists of many particles. These shape requirements also remove photons and electrons. These requirements are highly efficient for the signal, and the remaining background is estimated to be <0.1%.

The measured p_T of each jet is corrected for calorimeter nonlinearity and energy lost in uninstrumented regions. These average jet-by-jet energy corrections do not correct the smearing (bin-to-bin migration) of jets due to the finite energy resolution. This smearing is determined using an iterative procedure. It is assumed that the particle-level physics (true) spectrum is described by the function

$$F(p_T, y) = N_0 \left(\frac{p_T}{100\,\mathrm{GeV}/c}\right)^{\alpha} \left(1 - \frac{2\,p_T\,\cosh(y_{\min})}{\sqrt{s}}\right)^{\beta} \exp(-\gamma p_T), \qquad 6.$$

where $y_{\min}$ is the rapidity lower bin edge. This functional form is a good representation of the NLO pQCD prediction and fits the measured raw inclusive jet spectrum well. This true spectrum is smeared using the jet energy resolution function, which is determined using $p\bar{p}$ collider dijet data and simulated dijet events. The resulting smeared spectrum is compared with data by use of a χ^2 test. The process is iterated to determine the best parameters (N_0, α, β, γ) of the true function, $F(p_T, y)$. This true spectrum is used to correct the migrations between bins in p_T in the observed data. In the central region, the migration correction is a multiplicative factor that is 0.8 to 0.9 at low p_T and 0.7 at high p_T, with a strong dependence on y. The true spectrum $F(p_T, y)$ is measured separately for each rapidity bin. The jet rapidity is measured very precisely, and thus migration between rapidity bins is small. The y migration corrections are less than 2% in most bins, and 10% in the highest-p_T bin, where the spectrum is the steepest. The rapidity unsmearing is applied after the p_T unsmearing. After the jet energy scale and resolution smearing corrections, the observed data distribution is corrected to the particle level and is completely independent of the detector properties.

The observed inclusive particle jet spectrum compared with the NLO pQCD predictions, corrected for underlying-event and hadronization effects, is shown in **Figure 3**. The NLO pQCD predictions are calculated by using NLOJet++ and FastNLO (17, 18), which use α_s^3 matrix elements with $\mu_R = \mu_F = p_T^{\mathrm{jet}}$. The PDFs from CTEQ6.5M (49), which include the Run I inclusive jet data, are used. The experimental uncertainty, dominated by the jet energy scale uncertainty, is 12% at $p_T = 50$ GeV/c and 17% at $p_T = 550$ GeV/c in the $|y| < 0.4$ bin. The uncertainty is higher in other y bins. These results are the most precise to date. The main theoretical uncertainties arise from the uncertainty on the PDFs and the missing higher-order terms in the perturbation series. As is customary, the effect of higher-order terms is evaluated by varying the renormalization and factorization scales. Fortunately, the change in cross section from varying these scales is almost independent of the p_T of the jets. The predicted cross section changed by ~10 to 15% when the scale was changed to $\mu_F = \mu_R = 2p_T$ or $\mu_F = \mu_R = p_T/2$. There is a good agreement between the data and the theoretical predictions over the whole p_T range, which spans 50 GeV/c to 550 GeV/c. Over this p_T range, the cross section falls by ten orders of magnitude.

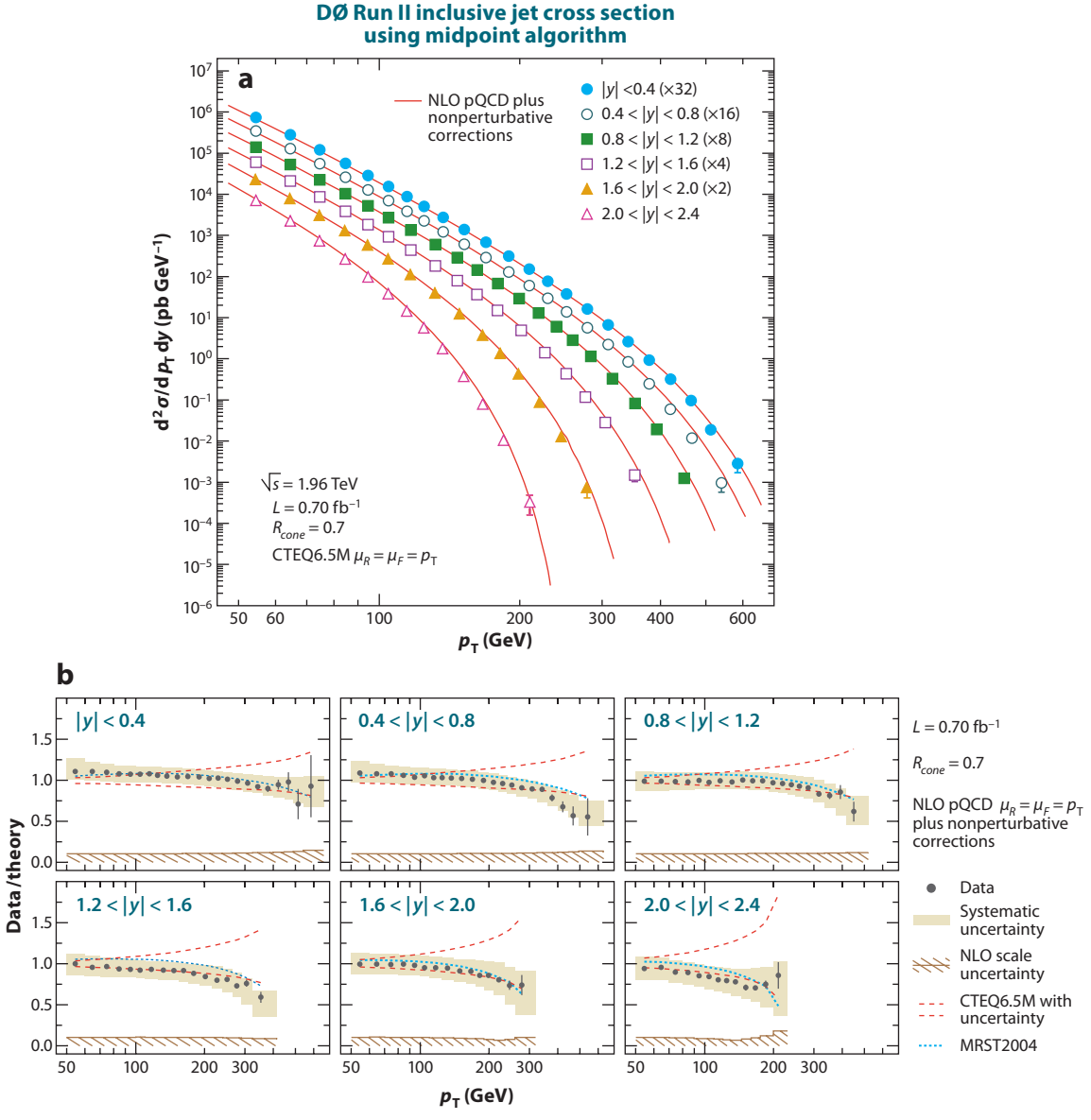

Figure 3

(*a*) DØ's observed inclusive jet differential cross sections corrected to the particle level in six rapidity regions compared to next-to-leading-order (NLO) quantum chromodynamics (QCD) predictions (48). The NLO QCD predictions are calculated with the CTEQ6.5M parton distribution functions. (*b*) Ratios of the measured cross sections over the NLO QCD predictions. The dashed blue curves show the NLO perturbative QCD (pQCD) prediction calculation that used MRST2004, divided by the same calculation that used CTEQ6.5M. The data agree with the theory quite well and have remarkably small systematic uncertainties.

The data prefer the lower bound of the theoretical prediction, favoring a smaller gluon content of the proton at high x. The theoretical uncertainty arising from the uncertainties in the PDFs is larger than the experimental uncertainties. These data, along with CDF inclusive jet data, have been used in the global fits to improve the precision of the gluon distribution function. The results of these fits are described in Section 5.3.

5.1.2. CDF Collaboration. The CDF Collaboration measured the inclusive jet cross section for a cone size of $R = 0.7$, using data corresponding to 1.13 fb^{-1} (46). The measurement spans five rapidity bins, $|y| < 0.1$, $0.1 < |y| < 0.7$, $0.7 < |y| < 1.1$, $1.1 < |y| < 1.6$, and $1.6 < |y| < 2.1$. These bins are matched to the CDF calorimeter structure (12) and thus are different from the binning used in DØ's analysis. The data were collected between 2002 and 2005 using jet triggers with four thresholds: 20, 50, 70, and 100 GeV/c. To prevent saturation of the data-acquisition system by jet triggers, only 1/808, 1/35, and 1/8 of lower-threshold triggers were recorded. An average correction is applied to the transverse energy of each jet to form the jet p_{T} spectrum, which was corrected for bin-to-bin migration of jets due to finite jet energy resolution. CDF used simulated events to evaluate the smearing corrections. The corrections depend on the shape of the true jet p_{T} spectrum and the jet energy resolution. A large sample of QCD jet events was generated using the PYTHIA event generator (8) and passed through the CDF detector simulation. The detector simulation was tuned to describe the single-particle response measured in $p\bar{p}$ collisions (37). These simulated data were analyzed with the same procedure as the one used for the real data to obtain the smeared spectrum. The bin-to-bin migration effect was determined by taking the ratio of the smeared jet spectrum and the particle jet spectrum. For this procedure to be valid, the smeared p_{T} spectrum of the simulated events must match the spectrum measured in data. The two spectra are very close, but not exactly the same. The simulated particle jet–smeared p_{T} spectrum was adjusted (reweighted) to force it to agree with the measured spectrum. Reweighting changes the unsmearing corrections by only a few percent. The unsmearing correction is <5% for $p_{\text{T}}^{\text{jet}} < 300$ GeV/c and increases to as much as 20% at $p_{\text{T}} = 500$ GeV/c.

The corrected jet p_{T} spectrum is compared to pQCD predictions evaluated with the FastNLO (18) program using the CTEQ6.1M PDFs (50). The renormalization and factorization scales (μ_R and μ_F) are chosen to be $p_{\text{T}}/2$—the same as those used in the global QCD analysis—to determine the PDFs (50). Use of $\mu_R = \mu_F = p_{\text{T}}^{\text{jet}}$ gives up to 10% smaller predictions in the cross section. The pQCD predictions are corrected for underlying-event and hadronization effects measured using the procedure described in Section 2. While clustering the partons produced by FastNLO, CDF used an ad hoc parameter, R_{sep}, which was introduced to mimic the split and merge procedure in iterative cone clustering algorithms (33). At order α_s^3, the final state can have up to three partons. Depending on their relative p_{T} and their separation in $y - \phi$ space, these partons can be clustered into two or three jets. Two partons are clustered into a single jet if they are within R from the jet centroid and within $R \times R_{sep}$ of each other. A value of $R_{sep} = 1.3$ is used in this calculation. A value of $R_{sep} = 2.0$ (i.e., the midpoint algorithm without R_{sep}) yields less than a 5% increase in cross section for NLO QCD predictions. As shown in **Figure 4**, the data are in good agreement with the theoretical predictions. The experimental uncertainty, dominated by the jet energy scale uncertainty, is comparable to the theoretical uncertainty, which in turn is dominated by the PDF uncertainty.

5.2. Measurement Using the k_{T} Clustering Algorithm

The k_{T} clustering algorithm, which combines objects in pairs to reconstruct a jet, is IR and collinear safe at all orders in perturbation. The CDF Collaboration (47) measured the inclusive jet cross

CDF Run II inclusive jet cross section using midpoint algorithm

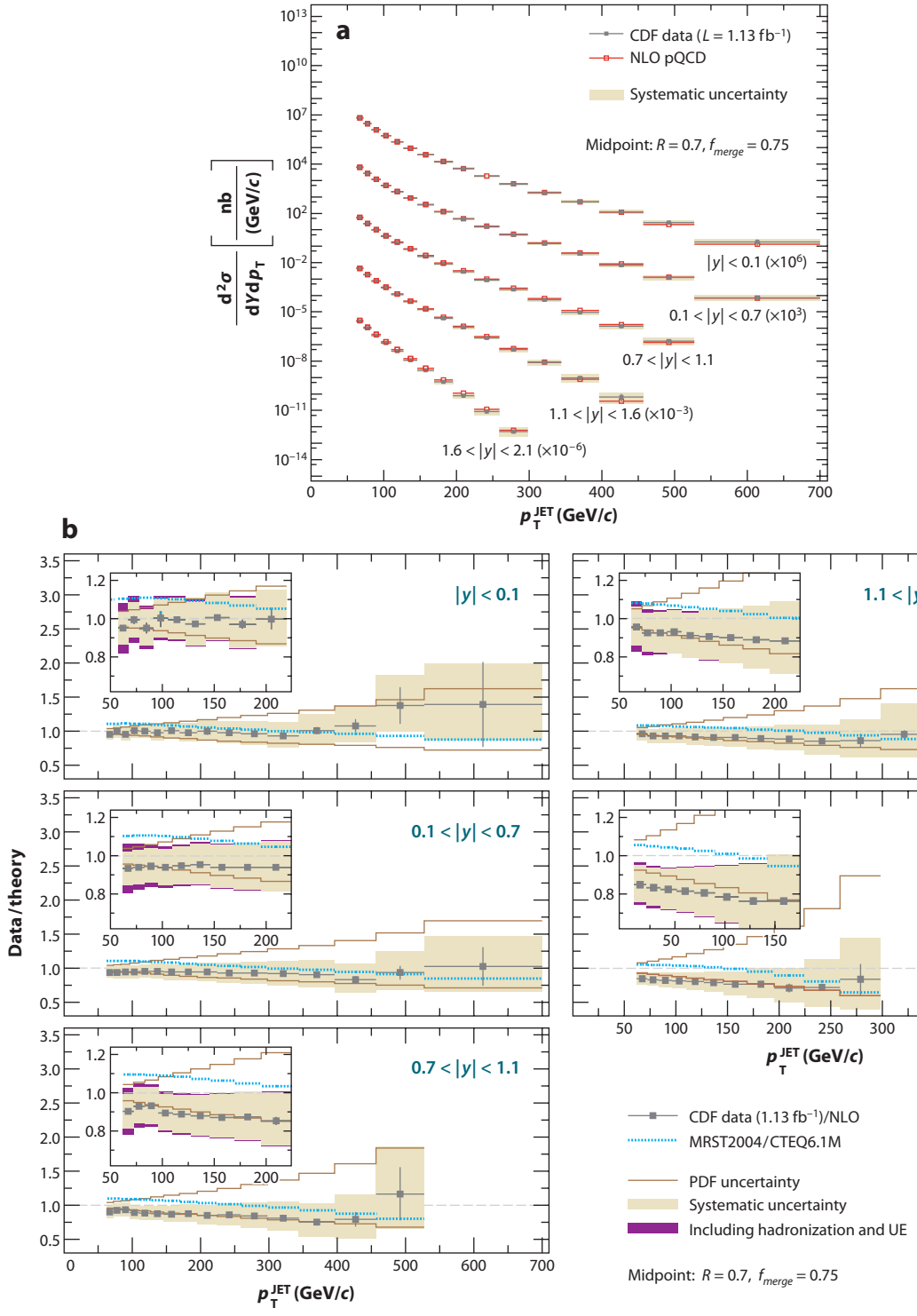

section by using the k_T clustering algorithm with $D = 0.4$, 0.7, and 1.0, using 1.0 fb^{-1} of data in the same rapidity region as in the cone-based analysis (46). The analysis procedure is similar to the one described in Section 5.1.2, except for the correction for multiple interactions, which are determined using a novel approach. The measured jet transverse momenta were corrected for this effect by removing a certain amount of transverse momentum, $\delta_{p_T}^{\text{mi}} \times (N_V - 1)$, where N_V denotes the number of primary vertices in the event. The value of $\delta_{p_T}^{\text{mi}}$ was determined by requiring the shape of the p_T spectrum at high instantaneous luminosity ($\mathcal{L}^{\text{inst}}$) to be the same as the one at low $\mathcal{L}^{\text{inst}}$. After the shape of two spectra were made the same, the data at low $\mathcal{L}^{\text{inst}}$ and high $\mathcal{L}^{\text{inst}}$ were combined. The study was carried out independently for each rapidity region, and the results were consistent with a common value of $\delta_{p_T}^{\text{mi}} = 1.86 \pm 0.23$ GeV/c. The corresponding correction for the cone jets is 0.97 ± 0.29 GeV/c, which is measured by summing the p_T in a cone of $R = 0.7$ in minimum bias events.

In **Figure 5** the p_T spectra are compared with NLO QCD predictions using the CTEQ6.1M PDFs (50), where $\mu = 0.5 \times p_T^{\text{max jet}}$ for $D = 0.7$. The theoretical predictions are calculated with the JETRAD (16) program. The data are in very good agreement with the QCD prediction except in the highest-rapidity bin ($1.6 < |y| < 2.1$), where the data are lower than the prediction but are well within experimental systematic uncertainties. The theoretical uncertainties are dominated by the PDF uncertainties and are comparable to or larger than the experimental uncertainties. The theoretical predictions using the MRST2004 PDFs are very close to those based on the CTEQ6.1M PDFs, except in the $1.6 < |y| < 2.1$ bin, where the MRST2004 cross section is smaller but still within the PDF uncertainty on the CTEQ6.1M prediction. The results for jet sizes $D = 0.5$ and $D = 1.0$ show similar behavior.

The jet p_T spectra measured using two different clustering algorithms are expected to be different and can be compared only via theoretical predictions. The ratios of data to theory from two analyses were compared; they are in very good agreement with each other except in the $0.7 < |y| < 1.1$ region, where the cross section measured using k_T is ~5% higher. In this y region, the CDF calorimeter coverage is not uniform, which leads to a large variation in calorimeter response and poor jet energy resolution. The two CDF analyses have similar experimental uncertainties. Thus, both the k_T and cone clustering algorithms can be successfully used at hadron colliders.

5.3. Determination of Gluon Distribution Function

The PDF $f_i(x, \mu)$, which is the probability of finding a parton with a type $i = g, q, \bar{q}$ with momentum fraction x and mass scale μ, must be experimentally determined. The PDFs for gluons, light quarks, and antiquarks ($u, d, s, \bar{u}, \bar{d}$, and $\bar{s}$) are normally determined from experimental data. For heavier quarks, namely c and b, they are normally dynamically generated through gluon splitting. Data from (*a*) $e^{\pm}p$ collisions at the ZEUS and H1 experiments (3); (*b*) νp, $\bar{\nu} p$, νn, and $\bar{\nu} n$ collisions at CCFR/NuTeV (52); (*c*) Drell-Yan (lepton pairs and W/Z bosons) production in pp (53) and $p\bar{p}$ collisions (54); (*d*) jet data from the Tevatron; and (*e*) many other experiments, especially low-energy experiments, are used to extract the PDFs using a global fit. These experiments are sensitive to different f_i. For example, $e^{\pm}p$ experiments are sensitive to the sum of the q and $\bar{q}$

Figure 4

(*a*) CDF's observed inclusive jet differential cross sections corrected to the particle level in five rapidity regions compared to next-to-leading-order (NLO) quantum chromodynamics (QCD) predictions (46). The NLO QCD predictions are calculated with the CTEQ6.1M parton distribution functions (PDFs). (*b*) Ratios of the measured cross sections over the NLO QCD predictions. The theory describes the data quite well. Abbreviations: pQCD, perturbative QCD; UE, underlying event.

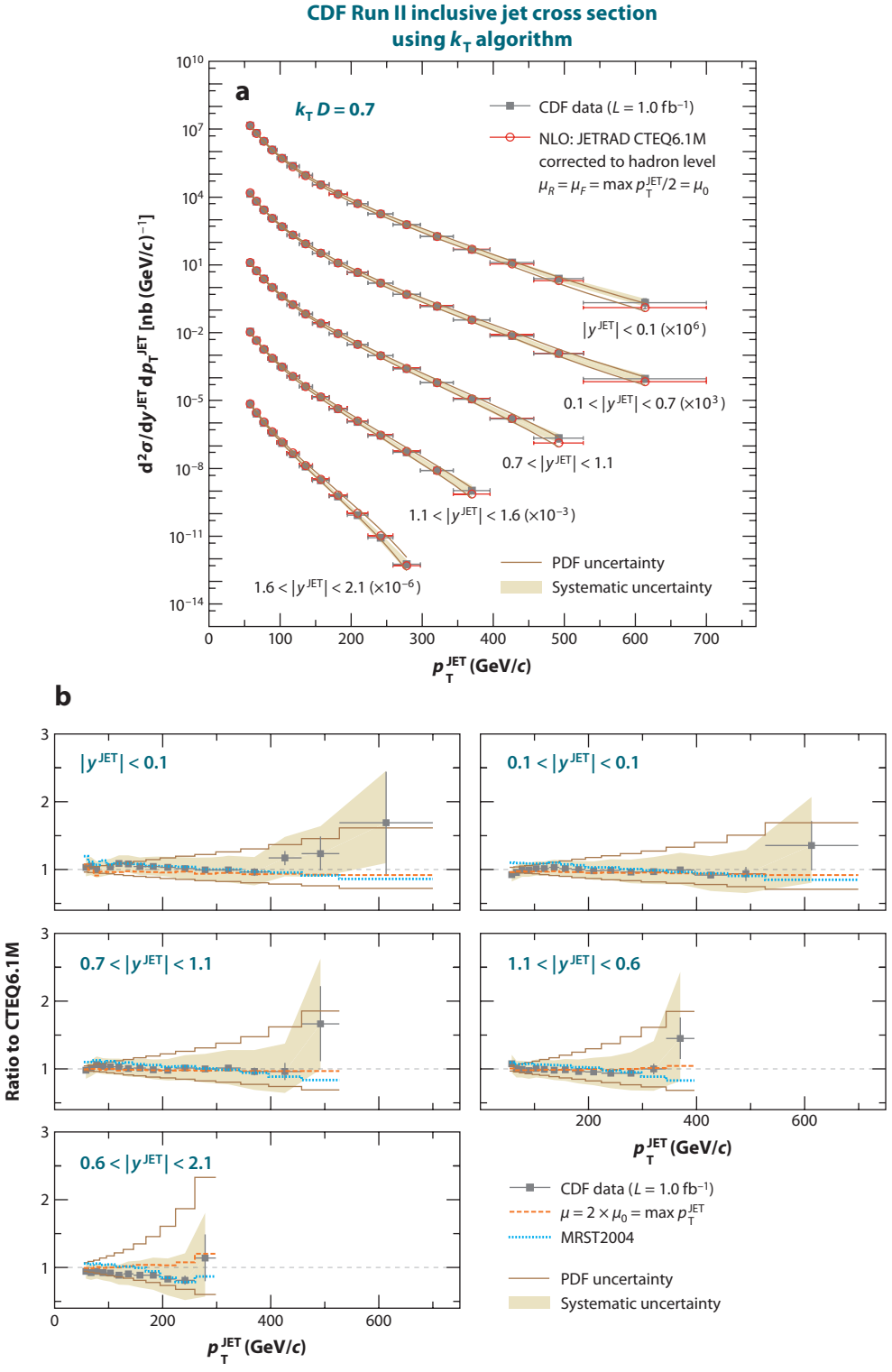

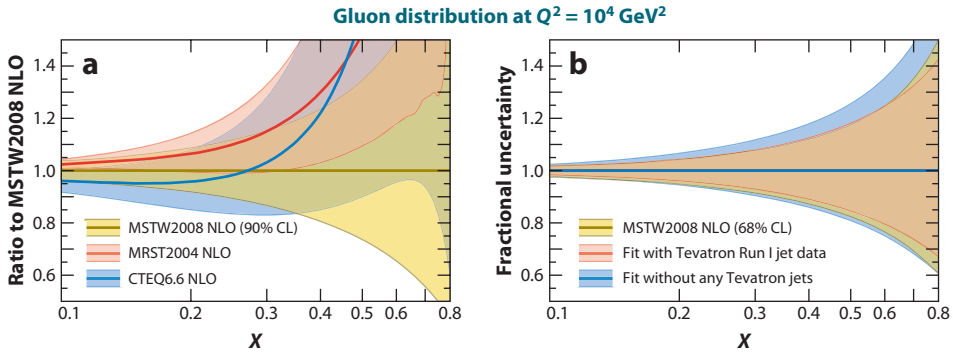

Figure 6

(*a*) Ratios of various gluon parton distribution functions (PDFs) to the MSTW2008 PDF. (*b*) The MSTW2008 gluon PDF uncertainties for variations on the inclusion or exclusion of Tevatron data (55). Abbreviation: NLO, next-to-leading order.

distributions weighted by $e^2_{q(\bar{q})}$ and cannot distinguish between quark and antiquark distributions. Neutrino and antineutrino data are used to differentiate between q and $\bar{q}$. The Tevatron jet data play a significant role in constraining the gluon distribution at high x. The gluon distribution at low x are determined mainly from the scaling violations in lepton-nucleon scattering data. Normally, the results of these global analyses are fit at some initial scale μ_0 using tens of parameters. The PDF can be evolved to any arbitrary scale μ using QCD evolution equations, which are available at NNLO approximation in perturbation theory.

Both the MSTW (55) and CTEQ (56) Collaborations have included Run II jet data in their global analysis to update the PDFs. The three Run II inclusive jet measurements are more accurate than Run I measurements, span a larger p_T range, and are consistent with each other (55). Because two CDF measurements used the same data, the MSTW Collaboration is using the k_T jet spectrum, whereas the CTEQ Collaboration is using the cone-based measurements. The Run I jet measurements do not play a significant role in the fit; thus, the MSTW Collaboration has dropped those data from the new fits. Comparisons between (*a*) the gluon distribution $g(x)$ determined in the new MSTW fit and (*b*) the gluon distributions from MRST2004 (57) and CTEQ6.6 (58) fits, along with the 90%-uncertainty band, are shown in **Figure 6*a*** for $\mu^2 = Q^2 = 10^4$ GeV^2. The new $g(x)$ is lower than previous fits for $x \geq 0.3$ but is within the still large systematic uncertainties. Because α_s and $g(x)$ always appear as a product, the values of α_s and $g(x)$ are strongly anticorrelated. The value of α_s in the three sets of PDFs is different, and thus $g(x)$ is also expected to be slightly different. The fractional uncertainty on the gluon distribution is shown in **Figure 6*b***. At $x = 0.4$ and $\mu^2 = 10^4$ GeV^2, the uncertainty reduces from 18%, when the jet data are excluded from the fit, to 12%, when jet data are included in the fit. This modest extra constraint will make the predictions more precise at the LHC in processes in which gluon-quark scattering dominates.

←

Figure 5

(*a*) CDF's inclusive jet differential cross sections measured using the k_T clustering algorithm in five rapidity regions. The data have been corrected to the particle jets and are compared to next-to-leading-order (NLO) quantum chromodynamics (QCD) predictions (47). The NLO QCD predictions are calculated with the CTEQ6.1M parton distribution functions (PDFs). (*b*) Ratios of the measured cross sections over the NLO QCD predictions. The perturbative NLO QCD calculations are in good agreement with the data.

5.4. Determination of the Strong Coupling Constant

The hard cross section for jet production ($\hat{\sigma}_{ij}$) in Equation 1 at high p_T can be expanded in powers of the strong coupling constant to the nth order in perturbation theory,

$$\hat{\sigma}_{ij} = \alpha_s^2 \sum_{m=0}^{n} c_{ij}^{(m)} \alpha_s^m, \qquad 7.$$

where the perturbative coefficients $c_{ij}^{(m)}$ are functions of the kinematic variables and the factorization and renormalization scales only. The coefficients $c_{ij}^{(m)}$ are available for $m = 0$ and $m = 1$. By use of the jet cross-section measurement, the strong coupling constant α_s can be determined with Equation 1, provided that the PDFs are known. This technique was used by the CDF Collaboration to measure α_s at different p_T values and show its running with the hard scattering scale in Run I (59). In Run II, the DØ Collaboration used the same principle but employed an improved technique to measure α_s (60) from the data used to measure the inclusive jet cross section. The hadronization and underlying-event corrections were determined using PYTHIA and applied to theoretical predictions. The hadronization (underlying-event) corrections vary from -15% ($+30\%$) to -3% ($+6\%$) for $p_T = 50$ GeV/c to 600 GeV/c (48).

The perturbative results are the sum of $\mathcal{O}(\alpha_s^3)$ pQCD calculations (17, 18), supplemented with $\mathcal{O}(\alpha_s^4)$ (two-loop) corrections for the threshold effects (19). The PDFs are taken from the MSTW2008 NNLO parameterization, and the renormalization and factorization scales are set to be equal to the p_T of the jet. The LO (NLO) MSTW2008 PDFs are available for 21 different values of $\alpha_s(Mz)$, ranging from 0.107 to 0.117 (0.110 to 0.130) in steps of 0.001. This α_s is used to evolve the PDFs.

Commonly available parton distributions from the MSTW and CTEQ groups include Tevatron jet data in the global fit. To avoid any correlation between the input PDFs and the extracted α_s, only 22 of the 110 available jet data points are used. These selected points contribute to the x region ($x \leq 0.25$), where PDFs in global fits are determined mainly by other experimental data and are not strongly influenced by Tevatron jet data. The jet data begin to affect $g(x)$ at $x \sim 0.2$. The change in $g(x)$ due to the inclusion of jet data is less than 5% for $x \lesssim 0.25$ (55).

The central $\alpha_s(Mz)$ result is obtained by minimizing the χ^2 with respect to $\alpha_s(M_Z)$ and by integrating over the nuisance parameters for the correlated uncertainties. The variation of $\alpha_s(p_T)$ versus p_T is shown in **Figure 7*a***. The running of α_s as a function of jet p_T follows the QCD evolution equation. The data points from the H1 and ZEUS experiments follow the same curve but have large uncertainties. The α_s, evolved to $\mu = M_Z$, is shown in **Figure 7*b***. The combined result of 22 selected points, $\alpha_s(M_Z) = 0.1161^{+0.0041}_{-0.0048}$, is consistent with the world average of 0.1184 ± 0.0007 (61), although the (mostly theoretical) uncertainties are large.

6. SEARCHES FOR PHYSICS BEYOND THE STANDARD MODEL USING JETS

Due to large theoretical and experimental uncertainties in the jet production rate, the high-p_T tail cannot be used to improve upon the current limits on new interactions (62). However, there are kinematic distributions from jet events that can be used to identify physics beyond the Standard Model. Below we describe these searches using the dijet mass spectrum and the dijet angular distributions. These searches are not very sensitive to the jet energy scale, PDFs, or renormalization or factorization scales.

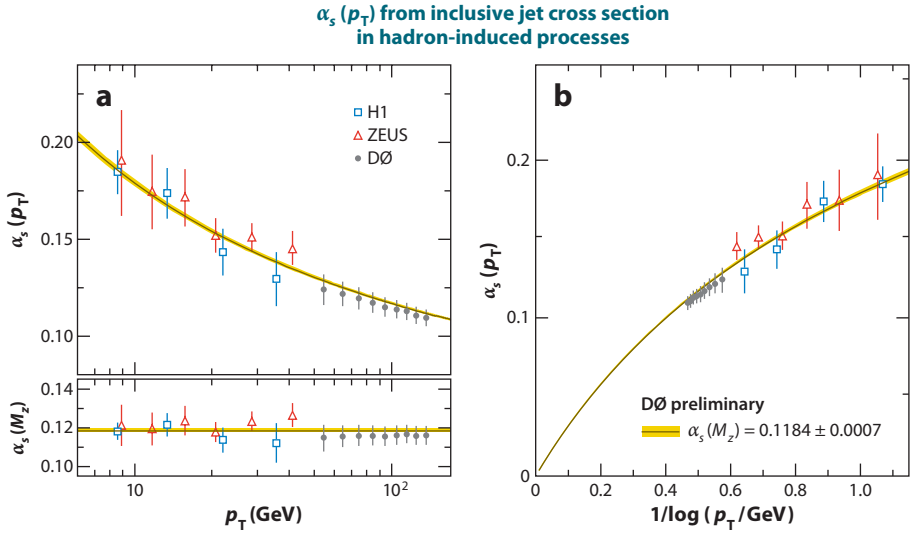

Figure 7

(*a*) Measurement of α_s as a function of the transverse momentum of the jet from several experiments, as compared to the expected variation of α_s. Here $\alpha_s(M_Z) = 0.1184 \pm 0.0007$ (60). (*b*) Plot of α_s as a function of 1/log (p_T), which supports the idea of asymptotic freedom.

6.1. Dijet Mass Spectrum

Many new physics models predict particles that decay into two high-p_T jets. Such particles can be identified by the reconstructed mass of the dijet system, provided that their intrinsic mass width is narrow. Such models include excited quarks (63), axigluons (64), flavor-universal colorons (65), color-octet techni-ρ (66), Randall-Sundrum gravitons (67), heavy vector bosons (68), and diquarks in the string-inspired E_6 model (69). The excited quarks q^* decay into qg. The heavy vector bosons W' and Z' decay into $q\bar{q}'$ or $q\bar{q}$, respectively. The axigluon A decays into $q\bar{q}$, and the E_6 diquarks D and D^c decay into $\bar{q}\bar{q}$ and qq, respectively. Both the Randall-Sundrum graviton G^* and the color-octet techni-ρ ρ_{T8} decay into either a $q\bar{q}$ or gg pair, but their branching ratios are different.

All these models predict an intrinsic mass width that is much smaller than both the detector resolution and the mass-broadening effects arising from QCD radiation. These models can be divided into three categories depending on the decay channel: gg, gq, and $q\bar{q}$. The expected mass shapes for q^*, G^*, W', and Z' particles with a mass of 800 GeV/c^2 are shown in **Figure 8**. Because q^* and G^* decay into gluons, their widths are broader than the widths of W' and Z'. Gluons radiate more than quarks, resulting in a broader dijet mass distribution. These distributions are close and change the final limits by only 10 to 20%. These shapes can be used to search for resonance structure, independent of the model details.

To measure the dijet mass spectrum (70), the CDF Collaboration used the same data set as in the inclusive jet cross-section measurement described in Section 5.1.2 (46). The dijet mass is reconstructed from the two highest-p_T jets using

$$m_{jj} = \sqrt{(E_1 + E_2)^2 - (\vec{p}_1 + \vec{p}_2)^2}. \qquad 8.$$

Jets produced by new physics are expected to be produced more centrally than by Standard Model processes, and we expect a better signal-to-background ratio in the central region. Thus, only those events in which two leading jets have $|y| \leq 1.0$ are used. Moreover, the CDF calorimeter

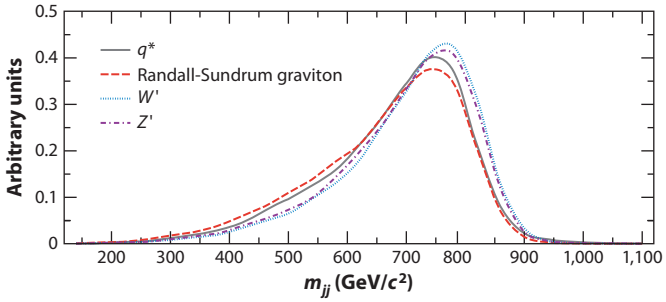

Figure 8

Expected dijet mass distributions for simulated signals for the following new physical models: $q^* \to qg$; Randall-Sundrum graviton $\to gg, q\bar{q}$; $W' \to q\bar{q}'$; and $Z' \to q\bar{q}$, where the particles have a mass of 800 GeV/c^2.

is best understood in this region. As shown in **Figure 9**, these data, after all corrections, are in good agreement with the NLO QCD calculations. The dijet mass spectrum before smearing corrections is shown in **Figure 10**. To guard against any theoretical biases, dijet resonance searches are performed without the use of smearing corrections. The measured mass spectrum is fit to a smooth background given by

$$\frac{d\sigma}{dm_{jj}} = p_0(1-x)^{p_1}/x^{p_2+p_3\ln(x)}, \quad x = m_{jj}/\sqrt{s}, \qquad 9.$$

where p_0, p_1, p_2, and p_3 are free parameters. The dijet mass spectra predicted by PYTHIA, HERWIG, and NLO pQCD can be described well by this functional form. The fit to the measured dijet mass spectrum is shown in **Figure 10*a***. The data are well described by this smooth function, with a χ^2

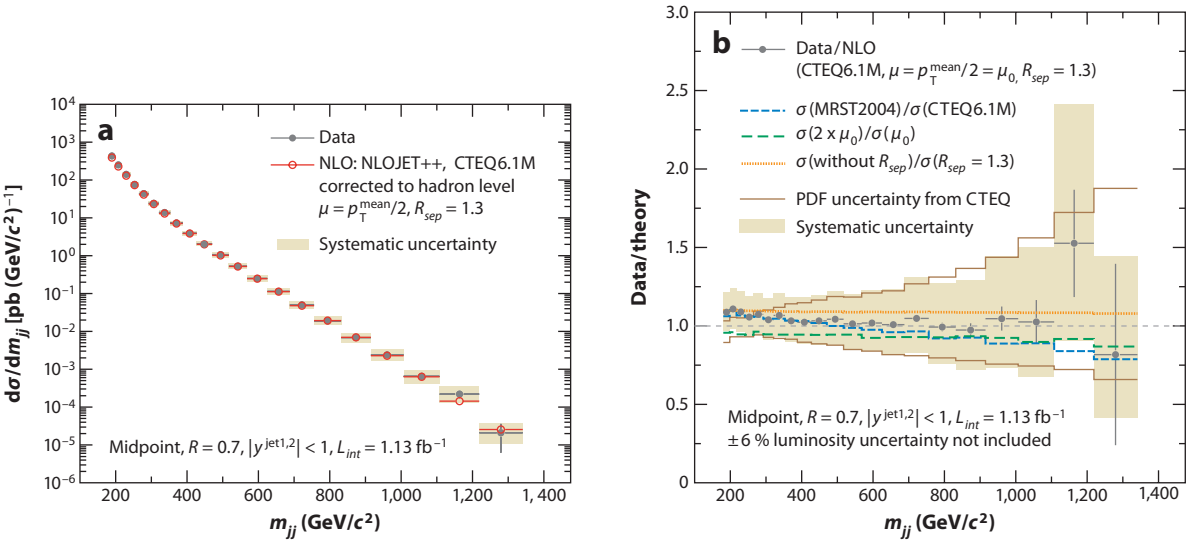

Figure 9

(*a*) CDF's measurement of the dijet mass cross section for events in which the two highest p_T have $|y| < 1.0$ (70), compared to next-to-leading-order (NLO) calculations by use of CTEQ6.1M. (*b*) Ratio of data to NLO theory. The experimental uncertainties are dominated by jet energy scale uncertainty and are comparable to the theoretical parton distribution function (PDF) uncertainty.

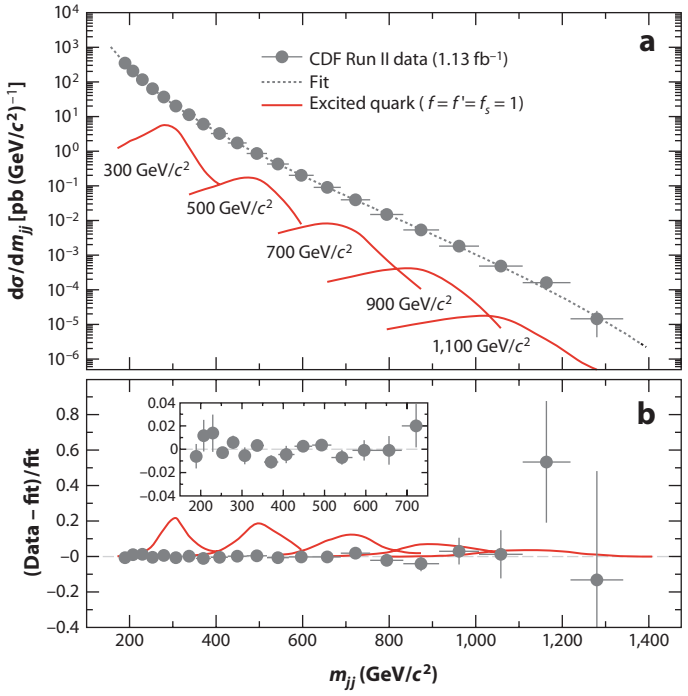

Figure 10

(*a*) CDF's measured dijet mass spectrum (70). The dashed gray curve shows the fit to Equation 9. Also shown are the predicted dijet mass distributions of the excited quark q^* for masses of 300, 500, 700, 900, and 1,100 GeV/c^2, respectively. (*b*) The fractional difference between the measured dijet mass difference and the fit (*points*) compared to q^* signals, divided by the fit to the measured dijet mass spectrum (*curves*).

of 16 for 17 degrees of freedom. The deviation from the smooth curve is shown in **Figure 10*b***. These data are used to determine the exclusion limits on the existence of new particles decaying into jets, as there is no evidence for the existence of any resonant structure. The experimental limits are determined for $\sigma^{sig} \equiv \sigma \times B \times A$, where σ is the theoretical new particle–production rate, B is the probability of the particle decaying into two jets, and A is the kinematic acceptance of the resulting particle jets to have $|y| < 1.0$.

The upper limits on σ^{sig} are evaluated using a likelihood function,

$$L = \prod_i \mu_i^{n_i} \exp(-\mu_i)/n_i!, \qquad 10.$$

where $\mu_i = n_i^{sig} + n_i^{QCD}$ is the predicted number of events in bin i. The QCD dijet background n_i^{QCD} is determined using Equation 9 by evaluating $\mathcal{L}_i \times \varepsilon_i \times \Delta m_{jj} \times d\sigma/dm_{jj}|_i$, where Δm_{jj}, ε_i, and $\mathcal{L}_i$, are the bin width, the trigger efficiency, and the integrated luminosity for bin i, respectively. The number of expected signal events n_i^{sig} is given by $\sigma^{sig} \times \mathcal{L}_i \times \varepsilon_i \times (n_i/n_{tot})$, where ε_i is the signal event–selection efficiency in the ith dijet mass bin and n_i/n_{tot} is the predicted signal fraction in bin i. For each value of σ^{sig}, the likelihood is maximized with respect to the four parameters in Equation 9. This profiled likelihood is integrated over Bayesian priors for the parameters describing the systematic uncertainties (71). A flat prior on σ^{sig} is used to extract a Bayesian upper limit on that parameter.

Table 1 The limits on the masses of particles decaying into dijets in various models[a]

Model	Parameters	Excluded region
q^*	$f = f' = f_s$	260–870
Axigluons		260–1,250
Coloron		290–630
E_6 diquark		260–1,100
ρ_{T8}		280–840
W'	Standard Model	280–840
Z'	Standard Model	320–740
G^*	$k/M_{Pl} = 0.1$	—

[a]Limits are in units of GeV/c^2 (70).

The mass exclusion limits for W', Z', q^*, and G^* are determined by comparing the limits obtained using their respective signal shapes and the predicted theoretical cross section. For other models, the limits obtained for these four signal shapes are used. The q^* signal shape (qg) is used for axigluons, the flavor-universal coloron, and the E_6 diquark, as these particles do not decay into modes that include gluons, and thus their signal shapes are expected to be narrower than that of q^*. For ρ_{T8}, the limits obtained for the G^* shape are used. Both the ρ_{T8} and the G^* decay into $q\bar{q}$ or gg, but the branching fraction of G^* into gg is higher. Therefore, in all the above cases, the obtained exclusion limits are conservative. The limits for these models are given in **Table 1**.

The dijet mass spectrum measured by the DØ Collaboration in six rapidity bins (72) is shown in **Figure 11**. The rapidity bin is labeled by the higher of the two jet rapidities. The data are compared to NLO pQCD predictions computed by NLOJet++ (17) using the MSTW2008 NLO PDFs (55) with scale $\mu_R = \mu_F = (p_{T,1} + p_{T,2})/2$ and are corrected for nonperturbative effects determined by using the PYTHIA event generator. The data and QCD predictions are in reasonable agreement for the $|y| < 0.4$ region, which is not surprising given that the MSTW2008 global fit includes the inclusive jet data (see Section 5.3). For higher $|y|$ bins, the data are below the theoretical predictions but are within 1σ of the total experimental systematic uncertainty. The DØ Collaboration is searching for new particles using these data.

6.2. Dijet Angular Distributions

The angle between the initial- and final-state partons in the center-of-momentum frame is sensitive to the spin of the exchanged or the intermediate particle and thus can be used to search for physics beyond the Standard Model. At hadron colliders, dijet production is dominated by the t channel exchange of a gluon, which is a massless vector boson, and the angular distribution has the familiar Rutherford scattering form

$$\frac{d\hat{\sigma}}{d\cos\theta^*} \sim \frac{1}{(1-\cos\theta^*)^2} = \frac{1}{\sin^4(\theta^*/2)}, \qquad 11.$$

where θ^* is the angle between the jet and the beam direction in the dijet center-of-momentum frame. The angular distribution of the new particles proposed in many new physics scenarios is

Figure 11

(*a*) DØ's dijet mass measurement for six rapidity bins (72) compared to next-to-leading order (NLO) using MSTW2008 PDFs. (*b*) Ratio of data to theory. The experimental systematic uncertainties are very small. The dashed red lines show the effect of using the CTEQ6.6M parton distribution functions (PDFs).

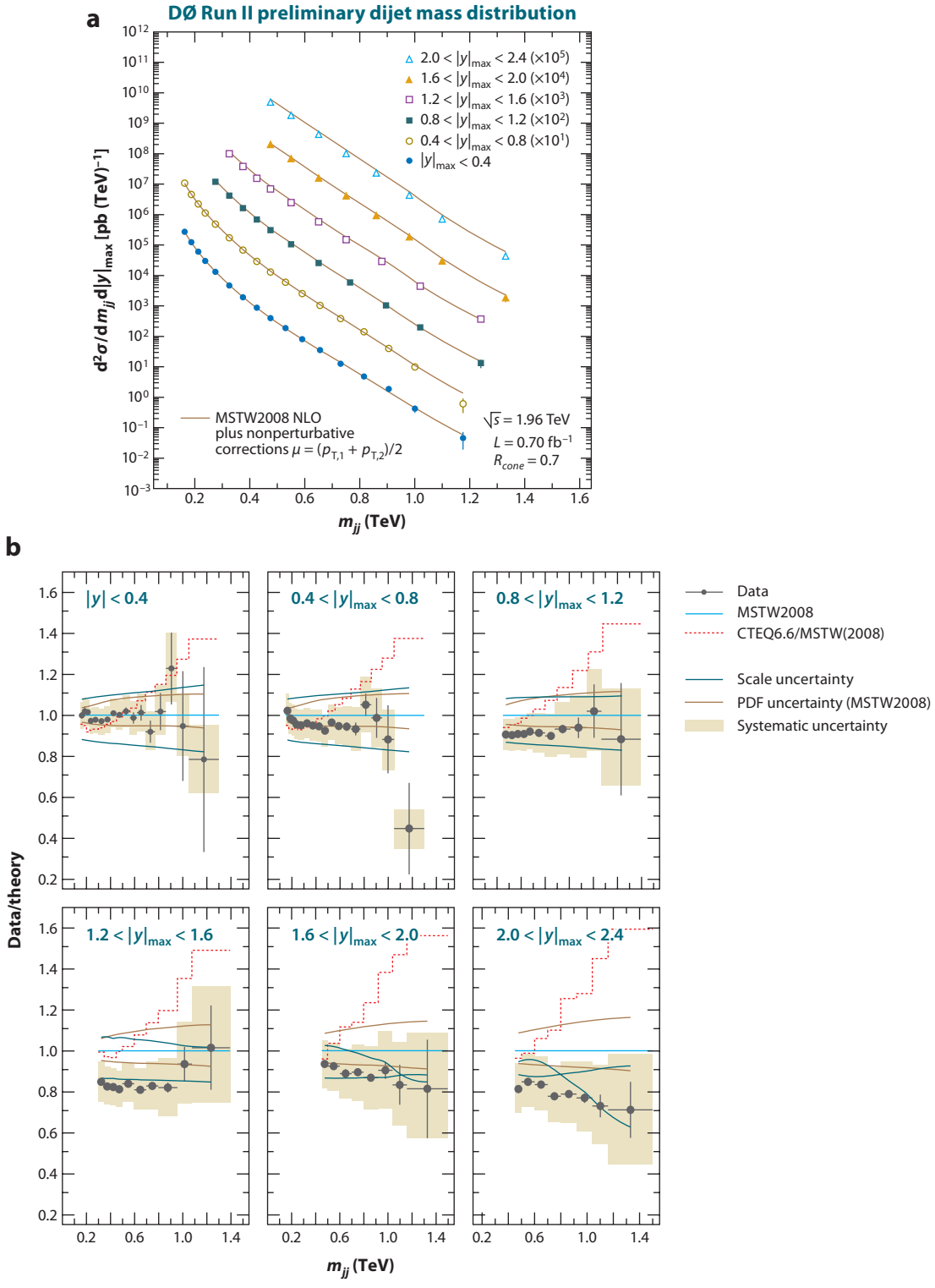

relatively flat in $\cos\theta^*$. For example, the angular distribution of spin-1 particles (W', Z', axigluon, coloron) decaying in fermions is $d\sigma/d\cos\theta^* \sim 1+\cos^2\theta^*$. Theories in which quarks are composite particles, but where the compositeness scale is much higher than the available energy, can be parameterized by an effective Lagrangian of the type (62, 73, 74)

$$\mathcal{L} = \eta \frac{g^2}{4\Lambda^2}(\bar{q}_i\gamma^\mu q_i)(\bar{q}_j\gamma_\mu q_j), \quad i = L, R;\ j = L, R,$$

where Λ is a parameter in the theory that controls the characteristic energy of the new interactions. The parameter η is ± 1 and determines the sign of interference between new interactions and the Standard Model interactions. The main effect of the substructure is to increase the proportion of centrally produced jets, which can be observed in the jet angular distributions (73).

The ADD LED (Arkani-Hamed–Dimopoulos–Dvali large extra dimensions) models (75, 76) that have been proposed to solve the hierarchy problem, namely the difference between the electroweak scale ($\sim$100 GeV) and the Planck scale M_{Pl} ($\sim 10^{19}$ GeV), assume the existence of extra spatial dimensions in which gravity is allowed to propagate. As a consequence, gravity appears weak in the three conventional spatial dimensions. The Planck scale, the number of extra dimensions n, their size R, and an effective Planck scale M_S are related by $M_{Pl} = M_S R^n$. Experimentally, M_S can be measured for different values of n. The Kaluza-Klein excitations of the graviton can be exchanged between partons and thus contribute to jet production, resulting in jets that are central. There are two different formalisms to describe LED models, GRW (Giudice-Rattazzi-Wells; 77) and HLZ (Han-Lykken-Zhang; 78). In the HLZ formalism, the subleading dependence on the number n of extra dimensions is also included.

In some models (79–81), extra dimensions are assumed to exist at the TeV^{-1} distance scale. In these models, Kaluza-Klein excitations of Standard Model bosons modify various production cross sections, and gluons can propagate through the extra dimensions, which changes the jet cross section. The strength of the interaction is given by the model parameter, the compactification scale M_C.

To search for new physics, instead of studying the $\cos\theta^*$ distribution directly it is convenient to use the χ_{dijet} distribution, which removes the Rutherford singularity: χ_{dijet} is defined as $\exp(y_1 - y_2)$, where y_1 and y_2 are rapidities (see footnote 1) of the two highest-p_T jets in an event. For $2 \to 2$ scattering of massless partons, the variable χ_{dijet} is related to the partonic center-of-momentum frame polar angle θ^* by $\chi_{dijet} = (1 + \cos\theta^*)/(1 - \cos\theta^*)$.

The CDF Collaboration studied the dijet angular distributions using 106 pb^{-1} of data from Run I (82). The data exclude at 95% CL a model of quark substructure in which only up and down quarks are composite and the contact interaction scale is $\Lambda^+_{ud} \leq 1.6$ TeV or $\Lambda^-_{ud} \leq 1.4$ TeV, where the subscript refers to the flavor of quarks assumed to be composite and the superscript $\pm$ refers to the sign of the interference. For a model in which all quarks are composite, the excluded regions are $\Lambda^+ \leq 1.8$ TeV and $\Lambda^- \leq 1.6$ TeV. In Run II, the DØ Collaboration measured the χ_{dijet} distribution in the $\chi_{dijet} \leq 16$ range in ten dijet mass m_{jj} bins covering the $0.25 < m_{jj} < 1.1$ TeV/c^2 range, using up to 0.7 fb^{-1} of data collected during 2004 and 2005 (83). The boost of the two-jet system is required to be $y_{\text{boost}} \equiv 0.5 \times |y_1 + y_2| \leq 1$. This requirement, combined with the dijet mass cut and the range of the χ_{dijet} distribution, restricts the highest allowable rapidity to $|y_{1,2}| < 2.4$, where the DØ detector performance is well understood. The measured distributions are corrected for detector effects using events generated with PYTHIA v6.419 (8) with Tune QW (21) and the MSTW2008 LO PDFs. This procedure corrects for the migration between dijet mass bins, as well as the shape of the χ_{dijet} distributions in each mass bin. The corrected normalized differential cross-section distributions ($1/\sigma_{dijet} \times d\sigma/d\chi_{dijet}$) at the particle level are shown in **Figure 12** for ten dijet mass bins. The NLO pQCD predictions are computed using

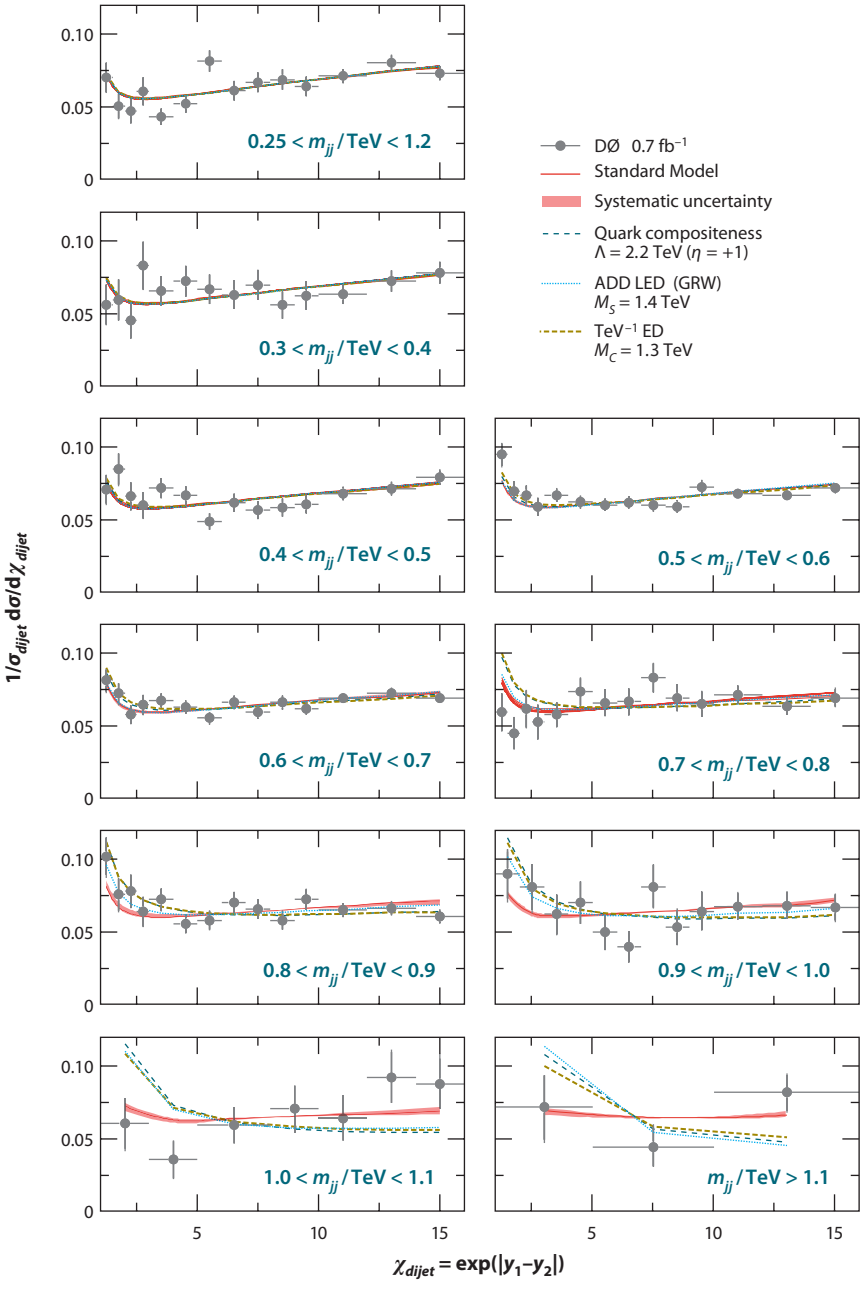

Figure 12

DØ's measurement of the dijet χ for ten dijet mass bins (83). The solid red line is the Standard Model prediction at next-to-leading order, and the shaded area shows the systematic uncertainty. The variously colored dashed lines show the predictions for various new physics models. Abbreviations: ADD LED, Arkani-Hamed–Dimopoulos–Dvali large extra dimensions; ED, extra dimensions; GRW, Giudice-Rattazzi-Wells.

Table 2 Expected and observed 95%-CL limits on various new physics models[a]

Model (parameter)	Expected (TeV)	Observed (TeV)
Quark compositeness (Λ)		
$\eta = +1$	2.76	2.84
$\eta = +-1$	2.75	2.82
TeV^{-1} ED (M_C)	1.60	1.55
ADD LED (M_S)		
GRW	1.47	1.59
HLZ $n = 3$	1.75	1.89
HLZ $n = 4$	1.47	1.59
HLZ $n = 5$	1.33	1.43
HLZ $n = 6$	1.24	1.34
HLZ $n = 7$	1.17	1.26

[a]Abbreviations: ADD, Arkani-Hamed–Dimopoulos–Dvali; ED, extra dimensions; GRW, Giudice-Rattazzi-Wells; HLZ, Han-Lykken-Zhang; LED, large extra dimensions.

FastNLO (18) based on NLOJet++ (17). These parton-level predictions are corrected for the hadronization and underlying-event contributions, which are evaluated using PYTHIA. The theoretical uncertainties on the Standard Model χ_{dijet} distributions arising from the uncertainty on the PDFs and the uncertainty on renormalization and factorization scales are less than 2% and 5%, respectively. These data are in good agreement with the Standard Model predictions and thus are used to set exclusion limits in the parameter space of quark compositeness, ADD LED, and TeV^{-1} models. Calculations for all these models are available only at LO, whereas pQCD calculations can be performed at NLO. For this analysis, the expected distributions for each new model are calculated at LO and then scaled by k-factors ($k = \sigma_{NLO}/\sigma_{LO}$) determined from pQCD calculations. The k-factors vary from 1.25 to 1.5. All these models predict a higher rate as $\chi_{dijet} \to 1$ and as m_{jj} increases. However, the magnitude of the excess is different for different models. A Bayesian procedure (45) is used to obtain 95%-CL limits on the mass scale parameters Λ, M_C, and M_S in the above models. The results in which the prior is chosen to be flat in the model cross section are given in **Table 2**. Other choices give similar but slightly higher limits (83).

The limits on M_C obtained in this analysis, although inferior to indirect limits from precision electroweak measurements (81), are the first direct search for TeV^{-1} extra dimensions at a particle collider. The limits on M_S in different formalisms of ADD LED are, on average, slightly higher than the recent DØ results obtained using dielectron and diphoton data (85). The quark compositeness limits are the most stringent limits to date.

7. CONCLUSIONS

Since the beginning of Run II, there has been a significant increase in the experimental data used in the jet analyses at the Tevatron. Due to the higher production cross section and the increase in available integrated luminosity, the inclusive jet cross-section measurement has been extended to transverse momenta of 600 GeV/c. The experimental uncertainty is still dominated by the uncertainty on the jet energy scale, which is $+31/-26\%$ in the $p_T = 457$–527 GeV/c bin in the $0.1 < |y| < 0.7$ region for CDF measurements and $+16.0/-15.5\%$ in the $p_T = 490$–540 GeV/c bin in the $|y| < 0.5$ region for DØ measurements. Both collaborations used a modern

jet-finding algorithm, the midpoint algorithm, which is IR and collinear safe at NLO in pQCD for measurements of the inclusive jet cross section. Also, the treatment of the underlying-event energy and hadronization effects has improved over the techniques used in Run I. The experimental uncertainties are lower than the theoretical uncertainties, which are dominated by the uncertainties on the PDFs. These data have been used in global fits to determine the parton distributions and have decreased the uncertainty on the gluon distribution for the $x \geq 0.3$ region. The new gluon distribution is slightly lower than that determined by Run I jet cross-section measurements. This increase in the accuracy of gluon distributions will make the prediction of various processes more precise.

These jet data have been successfully used to search for physics beyond the Standard Model via jet kinematic distributions. The dijet mass spectrum has been used to expand the exclusion regions in parameters of excited quarks in quark compositeness models, E_6 diquarks, axigluons, and heavy vector W and Z bosons, as well as the techni-ρ in color-octet models. The 95%-CL lower mass limits range from 630 GeV/c^2 for colorons to 1.25 TeV/c^2 for axigluons. The dijet angular distribution has been used to extend the limits on the quark compositeness mass scale, the ADD LED, and the TeV^{-1} extra dimensions. The 95%-CL lower limit on the compositeness mass scale is 2.8 TeV, and the 95%-CL lower limit for the compactification mass scale in the TeV^{-1} model is 1.5 TeV. The limits on the ADD LED range from 1.9 TeV to 1.3 TeV, depending on the number of extra dimensions in the HLZ formalism. The 95%-CL lower limit in the GRW formalism is 1.6 TeV. In most cases, these are the best limits to date.

DISCLOSURE STATEMENT

The authors are not aware of any affiliations, memberships, funding, or financial holdings that might be perceived as affecting the objectivity of this review.

ACKNOWLEDGMENTS

We thank Andrew Beretvas, Kenichi Hatakeyama, Markus Wobisch, and Marek Zielinski for reading the manuscript and for insightful comments.

LITERATURE CITED

1. Gross DJ, Wilczek F. *Phys. Rev. D* 8:3633 (1973); Fritzsch H, Gell-Mann M, Leutwyler H. *Phys. Lett.* B47:365 (1973); Politzer HD. *Phys. Rev. Lett.* 30:1346 (1973)
2. Stenzel H. *Nucl. Phys. B* 152:23 (2006)
3. Gwenlan C. *Acta Phys. Polon. B* 35:377 (2004)
4. Fabjan C, McCubbin N. *Phys. Rep.* 403:165 (2004)
5. Blazey GC, Flaugher BL. *Annu. Rev. Nucl. Part. Sci.* 49:633 (1999)
6. Salam GP. arXiv:0906.1736v3 [hep-ph] (2009)
7. Gribov VN, Lipatov LN. *Sov. J. Nucl. Phys.* 15:438 (1972); Altarelli G, Parisi G. *Nucl. Phys. B* 126:298 (1977); Dokshitzer Y. *Sov. Phys. JETP* 46:641 (1977)
8. Sjöstrand T, et al. *J. High Energy Phys.* 0605:026 (2006)
9. Corcella G, et al. *J. High Energy Phys.* 0101:010 (2001)
10. Frixione S, Webber BR. *J. High Energy Phys.* 0206:29 (2002)
11. Bhat CM. *Int. J. Mod. Phys. A* 16S1C:1187 (2001)
12. Abulencia A, et al. *J. Phys. G* 34:2457 (2007)
13. Abazov VM, et al. *Nucl. Instrum. Methods A* 565:463 (2006)
14. Ellis RK, Stirling WJ, Webber BR. *QCD and Collider Physics*. Cambridge, UK: Cambridge Univ. Press. (1996)

15. Ellis SD, Kunszt Z, Soper DE. *Phys. Rev. Lett.* 64:2121 (1990)
16. Giele WT, Glover EWN, Kosower DA. *Nucl. Phys. B* 403:633 (1993)
17. Nagy Z. *Phys. Rev. D* 68:094002 (2003)
18. Kluge T, Rabbertz K, Wobisch M. arXiv:hep-ph/0609285 (2006)
19. Kidonakis N, Owens JF. *Phys. Rev. D* 63:054019 (2001)
20. Field R. Presented at Fermilab ME/MC Workshop, Fermilab, Batavia, Ill. **http://www.phys.ufl.edu/~rfield/cdf/FNAL_Workshop_10-4-02.pdf** (2002)
21. Field R, et al. (Tev4LHC QCD Work. Group) arXiv:hep-ph/0610012 (2006)
22. Mangano ML, et al. *J. High Energy Phys.* 0307:001 (2003)
23. Gleisberg T, et al. *J. High Energy Phys.* 0402:056 (2004)
24. Catana S, Krauss F, Kuhn R, Webber BR. *J. High Energy Phys.* 0111:063 (2001); Krauss F. *J. High Energy Phys.* 0208:015 (2002)
25. Ellis SD, et al. *Prog. Part. Nucl. Phys.* 60:484 (2008)
26. Blazey GC, et al. arXiv:hep-ex/0005012v2 (2000)
27. Kilgore W, Giele WT. *Phys. Rev. D* 55:7183 (1997)
28. Buttar C, et al. arXiv:0803.0678v1 [hep-ph] (2008)
29. Salam GP. arXiv:0906.1833v1 [hep-ph] (2009)
30. Huth JE, et al. *FERMILAB-CONF-90-249-E* (1990)
31. Salam GP, Soyez G. *J. High Energy Phys.* 0705:086 (2007)
32. Catani S, et al. *Nucl. Phys. B* 406:187 (1993)
33. Ellis SD, Soper DE. *Phys. Rev. D* 48:3160 (1993)
34. Abazov VM, et al. *Phys. Lett.* B525:211 (2002)
35. Dokshitzer Yu, Leder G, Moretti S, Webber B. *JHEP* 9708:001 (1997); Wobisch M, Wengler T. arXiv:hep-ph/9907280 (1999)
36. Cacciari M, Salam GP, Soyes G. *J. High Energy Phys.* 0804:063 (2008)
37. Bhatti A, et al. *Nucl. Instrum. Methods A* 556:375 (2006)
38. Voutilainen M. *FERMILAB-THESIS-2008-19* (2008)
39. Amsler C, et al. *Phys. Lett.* B667:1 (2008)
40. Arnison G, et al. *Phys. Lett.* B172:461 (1986)
41. Alitti J, et al. *Phys. Lett.* B257:232 (1991); Alitti J, et al. *Z. Phys. C* 49:17 (1991)
42. Abe F, et al. *Phys. Rev. Lett.* 70:1376 (1993)
43. Abe F, et al. *Phys. Rev. Lett.* 77:438 (1996)
44. Affolder T, et al. *Phys. Rev. D* 64:032001 (2001)
45. Abbott B, et al. *Phys. Rev. D* 64:032003 (2001)
46. Aaltonen T, et al. *Phys. Rev. D* 78:052006 (2008)
47. Abulencia A, et al. *Phys. Rev. D* 75:092006 (2007)
48. Abazov VM, et al. *Phys. Rev. Lett.* 101:062001 (2008)
49. Tung WK, et al. *J. High Energy Phys.* 02:053 (2007); Pumplin J, et al. *J. High Energy Phys.* 07:12 (2002)
50. Stump D, et al. *J. High Energy Phys.* 10:046 (2003)
51. Deleted in proof
52. Tzanov M. *Int. J. Mod. Phys. A* 20:3759 (2005)
53. Towell RS, et al. *Phys. Rev. D* 64:052002 (2001)
54. Abe F, et al. *Phys. Rev. Lett.* 81:5754 (1998); Aaltonen T, et al. *Phys. Rev. Lett.* 102:181801 (2009); Aaltonen T, et al. arXiv:0908.3914v3 [hep-ex] (2009); Abazov VM, et al. *Phys. Rev. D* 76:012003 (2007)
55. Martin AD, et al. *Eur. Phys. J. C* 63:189 (2009)
56. Pumplin J, et al. arXiv:0904.2424v2 [hep-ph] (2009)
57. Martin AD, Roberts RG, Stirling WJ, Thorn RS. *Phys. Lett.* B604:61 (2004)
58. Nadolsky PM, et al. *Phys. Rev. D* 78:013004 (2008)
59. Affolder T, et al. *Phys. Rev. Lett.* 88:042001 (2002)
60. Abazov VM, et al. arXiv:0911.2710 [hep-ex] (2009)
61. Bethke S. *Eur. Phys. J C* 64:689 (2009)
62. Eichten E, Lane K, Peskin M. *Phys. Rev. Lett.* 50:811 (1983)

63. Baur U, Hinchliffe I, Zeppenfeld D. *Int. J. Mod. Phys. A* 2:1285 (1987); Baur U, Spira M, Zerwas PM. *Phys. Rev. D* 42:815 (1990)
64. Frampton PH, Glashow SL. *Phys. Lett.* B190:157 (1987); Bagger J, Schmidt C, King S. *Phys. Rev. D* 37:1188 (1988)
65. Chivukula RS, Cohen AG, Simmons EH. *Phys. Lett.* B380:92 (1996); Simmons EH. *Phys. Rev. D* 55:1678 (1997)
66. Lane KD, Ramana MV. *Phys. Rev. D* 44:2678 (1991); Lane K, Mrenna S. *Phys. Rev. D* 67:115011 (2003)
67. Randall L, Sundrum R. *Phys. Rev. Lett.* 83:3370 (1999); Bijnens J, et al. *Phys. Lett.* B503:241 (2001)
68. Eichten E, Hinchliffe I, Lane K, Quigg C. *Rev. Mod. Phys.* 56:579 (1984); Eichten E, Hinchliffe I, Lane K, Quigg C. *Rev. Mod. Phys.* 58:1065 (1986)
69. Hewett JL, Rizzo TG. *Phys. Rep.* 183:193 (1989)
70. Aaltonen T, et al. *Phys. Rev. D* 72:112002 (2009)
71. Demortier L. Presented at Conf. Adv. Stat. Tech. Part. Phys., Durham, UK (2002)
72. DØ Collab. *DØ Note 5919-Conf.* **http://www-d0.fnal.gov/Run2Physics/WWW/results/prelim/QCD/Q14/Q14.pdf** (2009)
73. Eichten E, Lane K. arXiv:hep-ph/9609298v1 (1996)
74. Lane KD. arXiv:hep-ph/9605257 (1996)
75. Arkani-Hamed N, Dimopoulos S, Dvali G. *Phys. Lett.* B429:263 (1998)
76. Atwood D, Bar-Shalom S, Soni S. *Phys. Rev. D* 62:056008 (2000)
77. Giudice GF, Rattazzi R, Wells JD. *Nucl. Phys. B* 544:3 (1999)
78. Han T, Lykken JD, Zhang RJ. *Phys. Rev. D* 59:105006 (1999)
79. Dienes KR, Dudas E, Gherghetta T. *Nucl. Phys. B* 537:47 (1999)
80. Pomarol A, Quiros M. *Phys. Lett.* B438:255 (1998)
81. Cheung K, Landsberg G. *Phys. Rev. D* 65:076003 (2002)
82. Abe F, et al. *Phys. Rev. Lett.* 77:5336 (1996)
83. Abazov VM, et al. *Phys. Rev. Lett.* 103:191803 (2009)
84. Deleted in proof
85. Abazov VM, et al. *Phys. Rev. Lett.* 102:051601 (2009)

Annual Review of Nuclear and Particle Science

Volume 60, 2010

Contents

Indexes

Errata

An online log of corrections to *Annual Review of Nuclear and Particle Science* articles may be found at http://nucl.annualreviews.org/errata.shtml